01 Jun 2022

On Internal Resonance Analysis of a Double-Cable-Stayed Shallow-Arch Model with Elastic Supports at Both Ends

Xiaoyang Su

Houjun Kang

Tieding Guo

Guirong Grace Yan
Missouri University of Science and Technology, yang@mst.edu

Recommended Citation

X. Su et al., "On Internal Resonance Analysis of a Double-Cable-Stayed Shallow-Arch Model with Elastic Supports at Both Ends," *Acta Mechanica Sinica/Lixue Xuebao*, vol. 38, no. 6, article no. 521475, Springer, Jun 2022.
The definitive version is available at https://doi.org/10.1007/s10409-022-21475-x

Springer

Acta Mechanica Sinica

CrossMark click for updates

•RESEARCH PAPER•

Acta Mech. Sin., Vol. 38, 521475 (2022)
https://doi.org/10.1007/s10409-022-21475-x

On internal resonance analysis of a double-cable-stayed shallow-arch model with elastic supports at both ends

Xiaoyang Su[1], Houjun Kang[1,2,3*], Tieding Guo[2,3], and Guirong Yan[4]

[1]*College of Civil Engineering, Hunan University, Changsha 410082, China;*
[2]*College of Civil Engineering and Architecture, Guangxi University, Nanning 530004, China;*
[3]*Scientific Research Center of Engineering Mechanics, Guangxi University, Nanning 530004, China;*
[4]*Department of Civil, Architectural and Environmental Engineering, Missouri University of Science and Technology, Rolla 65401, USA*

Received January 6, 2022; accepted March 18, 2022; published online April 21, 2022

In previous research on the nonlinear dynamics of cable-stayed bridges, boundary conditions were not properly modeled in the modeling. In order to obtain the nonlinear dynamics of cable-stayed bridges more accurately, a double-cable-stayed shallow-arch model with elastic supports at both ends and the initial configuration of bridge deck included in the modeling is developed in this study. The in-plane eigenvalue problems of the model are solved by dividing the shallow arch (SA) into three partitions according to the number of cables and the piecewise functions are taken as trial functions of the SA. Then, the in-plane one-to-one-to-one internal resonance among the global mode and the local modes (two cables' modes) is investigated when external primary resonance occurs. The ordinary differential equations (ODEs) are obtained by Galerkin's method and solved by the method of multiple time scales. The stable equilibrium solutions of modulation equations are obtained by using the Newton-Raphson method. In addition, the frequency-/force-response curves under different vertical stiffness are provided to study the nonlinear dynamic behaviors of the elastically supported model. To validate the theoretical analyses, the Runge-Kutta method is applied to obtain the numerical solutions. Finally, some interesting conclusions are drawn.

Cable-stayed bridge, Internal resonance, Vertical elastic support, Eigenvalue, Nonlinear vibration

Citation: X. Su, H. Kang, T. Guo, and G. Yan, On internal resonance analysis of a double-cable-stayed shallow-arch model with elastic supports at both ends, Acta Mech. Sin. **38**, 521475 (2022), https://doi.org/10.1007/s10409-022-21475-x

1. Introduction

Due to their long span, low damping and light weight, cable-stayed bridges are prone to severe vibrations under environmental excitations [1]. In some extreme situations, large nonlinear vibrations take place and they adversely affect the performance of bridges. Last year, Humen Bridge in Guangdong Province suffered large vortex-induced vibrations under winds, which seriously affected the comfort and safety of drivers. Actually, when nonlinear vibrations occur, the natural frequencies and mode shapes of the bridge system are not independent of vibration amplitude as in linear theory. Instead, if the vibration amplitude is large enough, natural frequencies and mode shapes depend on vibration amplitude [2]. To improve the performance of long-span cable-stayed bridges, it is imperative to systematically investigate the nonlinear dynamics of this type of bridge.

To study the nonlinear dynamics of a cable-stayed bridge, it is important to properly model the bridge itself [3]. Some studies modeled the entire bridge using a single cable [4,5] or beam [6-10], while others modeled it using a cable-stayed beam [11]. The cable-stayed beam model was firstly developed by Fujino and co-workers [12]. They established a 3DOF model that considered horizontal and vertical displacements of the beam and horizontal displacement of the cable. Thereafter, a lot of research was conducted based on a cable-stayed beam model. Gattuli and co-workers [13-15] carried out systematic studies on a cable-stayed beam. They conducted a parametric investigation of linear and nonlinear

*Corresponding author. E-mail address: HJKang@gxu.edu.cn (Houjun Kang)
Executive Editor: Rui Huang

behaviors in a cable-stayed beam and revealed how the mechanical characteristics affected the occurrence of global, local and coupled modes. They found that particular combinations of parameters would lead to a veering phenomenon between global and local frequencies. Through modal testing in the lab, Caetano et al. [16,17] studied the dynamic interaction between cables and deck/towers under the excitation from the seismic recordings. The results demonstrated that dynamic cable interactions with deck/towers and cable interference reduced bridge responses. Fung et al. [18] investigated the nonlinear vibration of cable-stayed bridges with time-varying length and tension. Wei et al. [19] analyzed the bifurcation and chaos phenomena of a cable-beam structure by including the comprehensive influence of nonlinear term caused by cable's sag and modal coupling of beam and cable. They pointed out that the structure exhibited different motions, such as chaotic motion or periodic and chaotic motions alternating, under different loading situations. Wang et al. [20] pointed out that the in-plane natural frequencies of a cable-stayed beam may include the contribution from the cable-deck interaction. By solving the eigenvalue problem, they found that the low-order out-of-plane natural frequencies were not affected by the cable-deck interaction and thus could be used to evaluate the cable force. Wang et al. [21] solved the in-plane and out-of-plane eigenvalue problems of a cable-stayed beam and studied the influence of the nonlinear coupling term on the dynamic characteristics of the cable-stayed beam.

Although previous research provided interesting results, the initial configuration of the bridge deck was not taken into consideration in the modeling. In practice, there is usually an initial camber to address the need of drainage in a cable-stayed bridge. This inspires many researchers to pay attention to the initial configuration (geometrical nonlinearity) of the bride deck [22]. Malhotra and Namachchivaya [23,24] investigated the chaotic motions of the shallow arch (SA) under one-to-one (and one-to-two) internal resonance. By considering the cable-deck interaction, a double-cable-stayed shallow-arch model was developed to model a cable-stayed bridge in Refs. [25,26], and the in-plane internal resonances of the system subjected to different external excitations were studied.

In addition, previous research assumed that the boundary conditions were ideal, either as hinged-hinged (H-H) ends or clamped-clamped (C-C) ends. In practice, boundary conditions are much more complex than this [27]. Leissa and Qatu [28] pointed out that even a steel beam perfectly welded to an infinitely large constraint block (i.e., an infinite half-space) would undergo rotation at the clamped end during vibration. Hence, elastic boundary conditions are more reasonable in reality [29]. By solving the eigenvalue equation, Yi et al. [30] proved that the elastic constraints had an influence on the natural frequency and mode shapes of the structural system, and there was a corresponding relationship with the coefficient of the modulation equation. Pi et al. [31] analyzed the nonlinear behaviors of elastically supported SAs. The results showed that the flexibility of the elastic supports and the shallowness of the arch implied an important influence on the nonlinear structural properties of the arch.

In order to obtain the nonlinear dynamics of a cable-stayed bridge more accurately, it is imperative to model the bridge as close to the real-world situation as possible. To bridge this research gap, a double-cable-stayed shallow-arch model with elastic supports at both ends and the initial configuration of the bridge deck included in the modeling is developed in this study. This research will explore the influence of proper modeling (using elastic supports to model boundary conditions and including the initial configuration of the bridge deck) on the dynamics of a cable-stayed bridge. As known, one-to-two and one-to-one internal resonances between the SA and the cable are the most common and possible resonance forms. As our present work, this paper is mainly concerned with one-to-one-to-one (two cables) internal resonance, which should be of great interest.

The remainder of this study is organized as follows. First, the cable-stayed shallow-arch model with proper boundary conditions and the initial configuration of the bridge deck is developed and the in-plane eigenproblem is solved by the separation-of-variable method. Then, the theoretical solution is derived. Discretization is conducted by applying Galerkin's method to get ordinary differential equations (ODEs) of the system and the corresponding modulation equations are acquired using the multiple timescale method. Next, the frequency-/force-response curves under different vertical stiffness are presented to explore the nonlinear dynamics of the model, and validation of the derivation of theoretical solutions is conducted. Finally, summary and conclusions are provided.

2. Modeling and planar eigenproblem solving

Figure 1 presents a simplified model consisting of a SA and two cables. In most references [32,33], the tower is usually considered to be rigid based on the fact that the vibration of the tower is very small compared with the beam and the cable. Hence, in Fig. 1, the two cables are fixed at one end and the other end is connected with the SA at s_1^* and s_2^*, respectively. The left cable is named as Cable 1, and the right is named as Cable 2. In order to model the boundary conditions more reasonably, the SA is constrained by four linear springs, namely, vertical springs with the stiffness of k_1^* and k_2^* and rotational springs with stiffness of k_3^* and k_4^*. It should be noted that the superscript "$*$" denotes the dimensional parameter. Two Cartesian coordinates soy and $x_jo_jy_j$

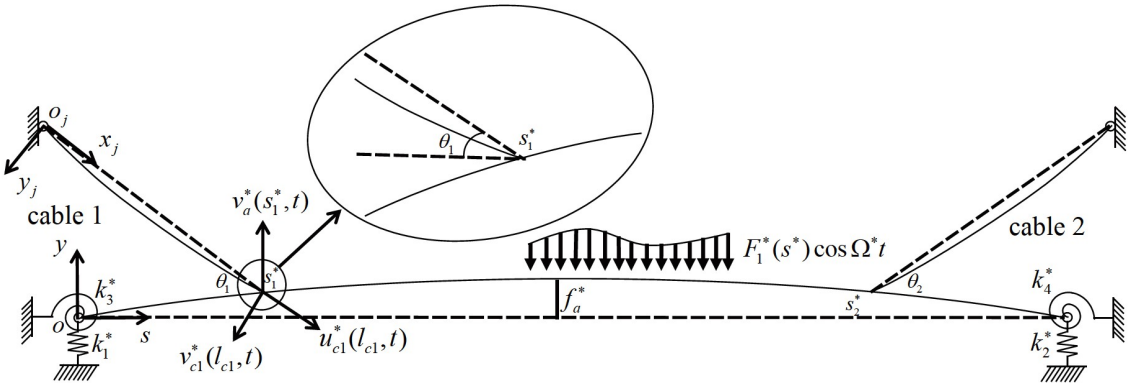

Figure 1 Double-cable-stayed shallow-arch model with elastic supports at both ends and initial configuration of bridge deck included.

(j = 1, 2, similarly hereinafter) are established, and in this way, the planar vibration of the model can be completely described by the SA transverse displacement v_a^* and the cable displacement components v_c^*, u_c^*. Additionally, subscript a denotes SA and c denotes cable. θ_j is the acute angle between the chord orientation of the cable and the horizontal line and f_a^* is the rise of the SA. In this study, the SA is assumed to be subjected to a distributed excitation, as shown in Fig. 1. $F_1^*(s^*)$ describes the spatial distribution of the harmonic load and Ω^* is the frequency. For the sake of derivation, the following assumptions are made.

(a) Ignore the actions of the tower on the model, that is, the tower is rigid.

(b) The sag-to-span ratio of the cable is small (≤1/10). In this case, the equilibrium configuration for the inclined cable can be approximated by the parabola [14]. Additionally, the flexural, shear and torsional rigidities of the cable are also negligible.

(c) The sag-to-span ratio of the SA is small (≤0.05). Hence, the initial deflection of the SA is described through a sinusoidal function [34]. Moreover, the shear and torsional rigidities of the SA are ignored.

(d) The axial vibration of the SA is ignored, as it is usually much smaller than transverse vibration. In addition, the influence of cable vibration on the axial motion of the SA is also neglected.

(e) The action of axial force of the cable on the SA is regarded as external loads, as seen in Eq. (2).

(f) The centerline stretching of the SA is related to its transverse displacement, which follows Ref. [34].

(g) The effects of the SA transverse movement on cable are assumed to be vertical dragging (perpendicular to *os*). In this regard, cable displacement contains two parts: one is the pure modal displacement, and the other is vertical dragging by the SA vibration.

According to the Hamilton's principle, the integral-differential equation governing the transverse vibration of the SA can be obtained as [24]:

$$E_a I_a v_a''''^* - E_a A_a \left[\frac{1}{L}\int_0^L \left(\frac{1}{2}v_a'^{2*} + y_a'^* v_a'^*\right) \mathrm{d}s^*\right] \cdot \left(v_a''^* + y_a''^*\right) + \mu_a^* v_{a,t}^* + \rho_a A_a v_{a,tt}^* = p_a^*(s^*, t), \tag{1}$$

where E, I, A, μ and ρ are Young's modulus, moment of inertia of the cross section, cross-sectional area, damping parameter and mass per unit length, respectively. L is the span of the SA. y_a^* is the initial deflection of the SA mentioned in assumption (b), and it is included in the equation to model the initial configuration of the SA. The comma preceding t in the subscript denotes differentiation with respect to t and the primes denote the differentiation with respect to coordinate s or x_j. p_a^* is the total loads acting on the SA, including the external load and the action of motion of cables, which can be written as:

$$p_a^*(s^*, t) = \sum_{j=1}^{2} \delta(s^* - s_j^*) E_{cj} A_{cj} e_{cj}^*(t) \sin\theta_j + F_1^*(s^*) \cos\Omega^* t, \tag{2}$$

where $\delta(s^* - s_j^*)$ is Kronecker delta function. e_{cj}^* denotes the uniform dynamic elongation of the jth cable and is given by

$$e_{cj}^*(t) = \frac{u_{cj}^*(l_{cj}, t)}{l_{cj}} + \frac{1}{l_{cj}}\int_0^{l_{cj}} \left(y_{cj}'^* v_{cj}'^* + \frac{1}{2}v_{cj}'^{2*}\right) \mathrm{d}x_j^*. \tag{3}$$

In Eq. (3), l_{cj} and y_{cj}^* denote the span and static equilibrium configuration of the jth cable, respectively.

Similarly, the differential equation governing the transverse vibration of the jth cable can be adopted from Ref. [14] and presented as:

$$\rho_{cj} A_{cj} v_{cj,tt}^* + \mu_{cj}^* v_{cj,t}^* - H_{cj} v_{cj}''^* - E_{cj} A_{cj} \left(v_{cj}''^* + y_{cj}''^*\right) e_{cj}^*(t) = 0, \tag{4}$$

where H_{cj} denotes the initial force of the jth cable.

From the Hamilton's variation procedure, the geometric and mechanical boundary conditions of cable and SA can also be obtained as follows:

$$v_{cj}(0,t)=0, \tag{5}$$

$$E_aI_av_a''^*(0,t)-k_3^*v_a'^*(0,t)=0, \tag{6}$$

$$E_aI_av_a''^*(L,t)+k_4^*v_a'^*(L,t)=0, \tag{7}$$

$$\begin{aligned}&E_aI_av_a'''^*(0,t)+k_1^*v_a^*(0,t)\\&-E_aA_a\left[\frac{1}{L}\int_0^L\left(\frac{1}{2}v_a'^{2*}+y_a'^*v_a'^*\right)\mathrm{d}s^*\right]\left[v_a'^*(0,t)+y_a'^*(0,t)\right]=0,\end{aligned} \tag{8}$$

$$\begin{aligned}&E_aI_av_a'''^*(L,t)-k_2^*v_a^*(L,t)\\&-E_aA_a\left[\frac{1}{L}\int_0^L\left(\frac{1}{2}v_a'^{2*}+y_a'^*v_a'^*\right)\mathrm{d}s^*\right]\left[v_a'^*(L,t)+y_a'^*(L,t)\right]=0.\end{aligned} \tag{9}$$

In Eqs. (8) and (9), the last term denotes the vertical component of the axial force of the SA, which can be neglected due to its small effect [27,35]. In addition, the displacements of the cable and SA at s_j should satisfy the following relationship:

$$v_a^*(s_j^*,t)\sin\theta_j+u_{cj}^*(l_{cj},t)=0, \tag{10}$$

$$v_a^*(s_j^*,t)\cos\theta_j+v_{cj}^*(l_{cj},t)=0. \tag{11}$$

Substituting Eq. (10) into Eq. (3) yields

$$e_{cj}^*(t)=-\frac{v_a^*(s_j^*,t)\sin\theta_j}{l_{cj}}+\frac{1}{l_{cj}}\int_0^{l_{cj}}\left(y_{cj}'^*v_{cj}'^*+\frac{1}{2}v_{cj}'^{2*}\right)\mathrm{d}x_j^*. \tag{12}$$

The following non-dimensional quantities are defined to deduce the dimensionless form of the equations of motion of this system:

$$\begin{aligned}&x_j=\frac{x_j^*}{l_{cj}},\tau=\omega_0t,y_{cj}=\frac{y_{cj}^*}{l_{cj}},v_{cj}=\frac{v_{cj}^*}{l_{cj}},\\&v_a=\frac{v_a^*}{L},\gamma_{cj}=\frac{L}{l_{cj}},s=\frac{s^*}{L},y_a=\frac{y_a^*}{L},\\&\mu_{cj}=\frac{\mu_{cj}^*}{\rho_{cj}A_{cj}\omega_0},\mu_a=\frac{\mu_a^*}{\rho_aA_a\omega_0},\Omega=\frac{\Omega^*}{\omega_0},\\&\beta_a^4=\frac{\rho_aA_a\omega_0^2L^4}{E_aI_a},\lambda_{cj}=\frac{E_{cj}A_{cj}}{H_{cj}},\beta_{cj}^2=\frac{\rho_{cj}A_{cj}\omega_0^2l_{cj}^2}{H_{cj}},\\&F_1(s)=\frac{F_1^*(s^*)}{\rho_aA_a\omega_0^2L},\psi_{cj}=\frac{E_{cj}A_{cj}}{\rho_aA_a\omega_0^2L^2},\eta=\frac{A_aL^2}{I_a},\\&k_1=\frac{k_1^*L^3}{E_aI_a},k_2=\frac{k_2^*L^3}{E_aI_a},k_3=\frac{k_3^*L}{E_aI_a},k_4=\frac{k_4^*L}{E_aI_a},\\&f_a=\frac{f_a^*}{L},\omega_0=1.0\ \mathrm{rad\ s^{-1}}.\end{aligned} \tag{13}$$

The resulting non-dimensional equations of motion are

$$\begin{aligned}&\frac{1}{\beta_a^4}v_a''''-\frac{\eta}{\beta_a^4}\left[\int_0^1\left(\frac{1}{2}v_a'^2+y_a'v_a'\right)\mathrm{d}s\right]\left(v_a''+y_a''\right)+\mu_av_{a,\tau}+v_{a,\tau\tau}\\&=\sum_{j=1}^{2}\delta(s-s_j)\psi_{cj}e_{cj}(\tau)\sin\theta_j+F_1\cos\Omega\tau,\end{aligned} \tag{14}$$

$$v_{cj,\tau\tau}+\mu_{cj}v_{cj,\tau}-\frac{1}{\beta_{cj}^2}\left[v_{cj}''+\lambda_{cj}\left(v_{cj}''+y_{cj}''\right)e_{cj}(\tau)\right]=0. \tag{15}$$

The non-dimensional linear forms of Eqs. (5)-(9) and (11) are

$$v_{cj}(0,\tau)=0, \tag{16}$$

$$v_a''(0,\tau)-k_3v_a'(0,\tau)=0, \tag{17}$$

$$v_a''(1,\tau)+k_4v_a'(1,\tau)=0, \tag{18}$$

$$v_a'''(0,\tau)+k_1v_a(0,\tau)-\eta\int_0^1y_a'v_a'\mathrm{d}s y_a'(0,\tau)=0, \tag{19}$$

$$v_a'''(1,\tau)-k_2v_a1,\tau)-\eta\int_0^1y_a'v_a'\mathrm{d}s y_a'(1,\tau)=0, \tag{20}$$

$$\gamma_{cj}v_a(s_j,\tau)\cos\theta_j+v_{cj}(1,\tau)=0. \tag{21}$$

The non-dimensional form of Eq. (12) is

$$e_{cj}(\tau)=-\gamma_{cj}v_a(s_j,\tau)\sin\theta_j+\int_0^1\left(y_{cj}'v_{cj}'+\frac{1}{2}v_{cj}'^2\right)\mathrm{d}x_j. \tag{22}$$

SA is divided into three segments according to the number of cables to obtain the mode shapes of the system. To conduct a modal analysis, the nonlinear, damping and excitation terms in Eqs. (14) and (15) are neglected and the linearized form of equations of motion for each SA segment and cable are obtained as:

$$\begin{aligned}&v_{ak}''''+\beta_a^4v_{ak,\tau\tau}\\&=\eta\left(\int_0^{s_1}y_a'v_{a1}'\mathrm{d}s+\int_{s_1}^{s_2}y_a'v_{a2}'\mathrm{d}s+\int_{s_2}^{1}y_a'v_{a3}'\mathrm{d}s\right)y_a'',\end{aligned} \tag{23}$$

$$\beta_{cj}^2v_{cj,\tau\tau}-v_{cj}''-\lambda_{cj}y_{cj}''\hat{e}_{cj}(\tau)=0, \tag{24}$$

where $k=1,2,3$, and

$$\hat{e}_{cj}(\tau)=v_{cj}(1,\tau)\tan\theta_j+\int_0^1y_{cj}'v_{cj}'\mathrm{d}x_j. \tag{25}$$

After the SA is segmented, the left and right sides of Node s_j shall match the following relationships.

(1) Mechanical equilibrium conditions:

$$\begin{aligned}&E_{aj}I_{aj}v_a'''^*(s_j^*,t)-E_{a(j+1)}I_{a(j+1)}v_{a(j+1)}'''^*(s_j^*,t)\\&+E_{cj}A_{cj}e_{cj}^*(t)\sin\theta_j+H_{cj}v'^*_{cj}(l_{cj},t)\cos\theta_j\\&+E_{cj}A_{cj}e_{cj}^*(t)\left[v'^*_{cj}(l_{cj},t)+y'^*_{cj}(l_{cj})\right]\cos\theta_j=0.\end{aligned} \tag{26}$$

The non-dimensional form of Eq. (26) can be written as:

$$\begin{aligned}&\chi_jv_a'''(s_j,\tau)-\chi_{j+1}v_{a(j+1)}'''(s_j,\tau)+\hat{e}_{cj}(\tau)\sin\theta_j\\&+\frac{1}{\lambda_{cj}}v_{cj}'(1,\tau)\cos\theta_j+\hat{e}_{cj}(\tau)y_{cj}'(1)\cos\theta_j=0,\end{aligned} \tag{27}$$

where $\chi_j=(E_{aj}I_{aj})/(L^2E_{cj}A_{cj})$ and $\chi_{j+1}=(E_{a(j+1)}I_{a(j+1)})/(L^2E_{cj}A_{cj})$.

(2) Displacement continuity conditions:

$$\begin{aligned} v_{aj}(s_j,\tau) &= v_{a(j+1)}(s_j,\tau),\ v'_{aj}(s_j,\tau) \\ &= v'_{aj(j+1)}(s_j,\tau),\ v''_{aj}(s_j,\tau) \\ &= v''_{a(j+1)}(s_j,\tau). \end{aligned} \tag{28}$$

To formulate the eigenvalue problem, the separation-of-variables method has been applied, i.e.,

$$v_{ak} = \phi_{ak}(s)\exp[\mathrm{i}(\omega/\omega_0)\tau],\ v_{cj} = \phi_{cj}(x_j)\exp[\mathrm{i}(\omega/\omega_0)\tau], \tag{29}$$

where i denotes $\sqrt{-1}$.

Based on assumption (b), the equilibrium equation of the cable can be expressed as:

$$y_{cj} = 4d_{cj}x_j(1-x_j), \tag{30}$$

where d_{cj} is rise-to-span ratio of the cable.

Substituting Eqs. (29) and (30) into (23)-(25) yields

$$\phi''''_{ak} - \overline{\beta}_a^4\phi_{ak} = \eta\left(\int_0^{s_1} y'_a\phi'_{a1}\mathrm{d}s + \int_{s_1}^{s_2} y'_a\phi'_{a2}\mathrm{d}s + \int_{s_2}^{1} y'_a\phi'_{a3}\mathrm{d}s\right)y''_a, \tag{31}$$

$$\overline{\beta}_{cj}^2\phi_{cj} + \phi''_{cj} = 8\lambda_{cj}d_{cj}\hat{e}_{cj}, \tag{32}$$

$$\hat{e}_{cj} = \phi_{cj}(1)\tan\theta_j + \int_0^1 y'_{cj}\phi'_{cj}\mathrm{d}x_j, \tag{33}$$

where $\overline{\beta}_a^4 = (\rho_a A_a\omega^2 L^4)/(E_a I_a)$ and $\overline{\beta}_{cj}^2 = (\rho_{cj}A_{cj}\omega^2 l_{cj}^2)/H_{cj}$.

The solutions for Eqs. (31) and (32) are well-known and they are expressed as:

$$\begin{aligned} \phi_{ak}(s) = {} & a_{k1}\cos\overline{\beta}_a s + a_{k2}\sin\overline{\beta}_a s \\ & + a_{k3}\cosh\overline{\beta}_a s + a_{k4}\sinh\overline{\beta}_a s + a_{k5}h, \end{aligned} \tag{34}$$

$$\phi_{cj}(x) = c_{j1}\sin\overline{\beta}_{cj}x + c_{j2}\cos\overline{\beta}_{cj}x + D_{jc}, \tag{35}$$

where h is a particular solution of Eq. (31), which can be taken as $h = \sin\pi s$ [36].

In Eq. (35), D_{jc} follows the following expression:

$$D_{jc} = \alpha_{j1}c_{j1} + \alpha_{j2}c_{j2}, \tag{36}$$

where

$$\begin{aligned} \alpha_{j1} = {} & \frac{8\lambda_{cj}d_{cj}}{\overline{\beta}_{cj}^2 - 8\lambda_{cj}d_{cj}\tan\theta_j} \\ & \cdot\left[4d_{cj}\left(\frac{2(1-\cos\overline{\beta}_{cj})}{\overline{\beta}_{cj}} - \sin\overline{\beta}_{cj}\right) + \sin\overline{\beta}_{cj}\tan\theta_j\right], \\ \alpha_{j2} = {} & \frac{8\lambda_{cj}d_{cj}}{\overline{\beta}_{cj}^2 - 8\lambda_{cj}d_{cj}\tan\theta_j} \\ & \cdot\left[\cos\overline{\beta}_{cj}\tan\theta_j - 4d_{cj}\left(1+\cos\overline{\beta}_{cj} - \frac{2\sin\overline{\beta}_{cj}}{\overline{\beta}_{cj}}\right)\right]. \end{aligned} \tag{37}$$

Meanwhile, substituting Eq. (29) into boundary, equilibrium and continuity conditions (Eqs. (16)-(21), (27) and (28)) yields

$$\phi_{c1}(0) = 0,\ \phi_{c2}(0) = 0, \tag{38}$$

$$\phi''_{a1}(0) - k_3\phi'_{a1}(0) = 0, \tag{39}$$

$$\phi''_{a3}(1) + k_4\phi'_{a3}(1) = 0, \tag{40}$$

$$\begin{aligned} & \phi'''_{a1}(0) + k_1\phi_{a1}(0) \\ & -\eta\left(\int_0^{s_1} y'_a\phi'_{a1}\mathrm{d}s + \int_{s_1}^{s_2} y'_a\phi'_{a2}\mathrm{d}s + \int_{s_2}^{1} y'_a\phi'_{a3}\mathrm{d}s\right)y'_a(0) = 0, \end{aligned} \tag{41}$$

$$\begin{aligned} & \phi'''_{a3}(1) - k_2\phi_{a3}(1) \\ & -\eta\left(\int_0^{s_1} y'_a\phi'_{a1}\mathrm{d}s + \int_{s_1}^{s_2} y'_a\phi'_{a2}\mathrm{d}s + \int_{s_2}^{1} y'_a\phi'_{a3}\mathrm{d}s\right)y'_a(1) = 0, \end{aligned} \tag{42}$$

$$\begin{aligned} & \gamma_{c1}\phi_{a1}(s_1)\cos\theta_1 + \phi_{c1}(1) = 0, \\ & \gamma_{c2}\phi_{a2}(s_2)\cos\theta_2 + \phi_{c2}(1) = 0, \end{aligned} \tag{43}$$

$$\begin{aligned} & \chi_1\phi'''_{a1}((s_1) - \chi_2\phi'''_{a2}(s_1) \\ & + \hat{e}_{c1}[\sin\theta_1 + y'_{c1}(1)\cos\theta_1] + \frac{1}{\lambda_{c1}}\phi'_{c1}(1)\cos\theta_1 = 0, \end{aligned} \tag{44}$$

$$\begin{aligned} & \chi_2\phi'''_{a2}(s_2) - \chi_3\phi'''_{a3}(s_2) \\ & + \hat{e}_{c2}[\sin\theta_2 + y'_{c2}(1)\cos\theta_2] + \frac{1}{\lambda_{c2}}\phi'_{c2}(1)\cos\theta_2 = 0, \end{aligned} \tag{45}$$

$$\phi_{a1}(s_1) = \phi_{a2}(s_1),\quad \phi_{a2}(s_2) = \phi_{a3}(s_2),\quad \phi'_{a1}(s_1) = \phi'_{a2}(s_1), \tag{46}$$

$$\phi'_{a2}(s_2) = \phi'_{a3}(s_2),\quad \phi''_{a1}(s_1) = \phi''_{a2}(s_1),\quad \phi''_{a2}(s_2) = \phi''_{a3}(s_2). \tag{47}$$

Equation (34) is required to satisfy Eq. (31), from which we can obtain three equations. Therefore, the 19 equations, including Eqs. (38)-(47), can be rewritten in the matrix form as:

$$\mathbf{TZ} = 0, \tag{48}$$

where $\mathbf{Z} = [c_{11}, c_{12}, c_{21}, c_{22}, a_{11}, \ldots, a_{15}, a_{21}, \ldots, a_{25}, a_{31}, \ldots, a_{35}]^{\mathrm{T}}$. And the elements in $\mathbf{T}$ are provided in Appendix A. According to the Cramer's Rule, if there are nontrivial solutions of Eq. (48), there must be

$$\Delta = |\mathbf{T}| = 0, \tag{49}$$

which is the eigenvalue equation of the system. With the help of numerical software, the numerical solutions of Eq. (49) can be easily obtained.

3. Perturbation technique and modulation equations

The process of solving the nonlinear system is tedious. Hence, for the sake of the reader's understanding, a flow chart is given as shown in Fig. 2. It should be noted that in this part, the model with only vertical elastic supports is taken as an example to discuss the nonlinear vibration of the system, since both vertical and rotational elastic supports essentially affect the nonlinear characteristics of the system by changing the shape function. Compared with multi-mode models, single-mode models are adopted when the concerned mode is not involved in an internal resonance with other modes, namely the response can be considered to consist of only the excited mode. This paper studied one-to-one-to-one internal resonance between the lowest modes of the shallow and cable. Hence, non-dimensional forms of the planar transverse displacements of the SA and cables can be expressed as:

$$v_a(s,\tau) = \phi_a(s)g(\tau), \tag{50}$$

$$v_{cj}(x_j,\tau) = -\gamma_{cj}v_a(s_j,\tau)x_j\cos(\theta_j) + \phi_{cj}(x_j)q_j(\tau), \tag{51}$$

where $\phi_a(s)$ and $\phi_{cj}(x_j)$ denote the mode shapes of the SA and the jth cable, respectively. $g(\tau)$ and $q_j(\tau)$ denote the corresponding generalized coordinates. Substituting Eqs. (50) and (51) into (14), (15) and (22) and applying the Galerkin discretization, the following ODEs are obtained:

$$\begin{aligned} &g_{,\tau\tau}+\mu_a g_{,\tau}+b_{11}g+b_{12}g^2+b_{13}g^3+b_{14}q_1+b_{15}gq_1+b_{16}q_2\\ &+b_{17}gq_2+b_{18}q_1^2+b_{19}q_2^2+b_{110}\cos(\Omega\tau)=0, \end{aligned} \tag{52}$$

$$\begin{aligned} &q_{j,\tau\tau}+\mu_{cj}q_{j,\tau}+b_{(j+1)1}g_{,\tau}+b_{(j+1)2}g_{,\tau\tau}+b_{(j+1)3}g+b_{(j+1)4}q_j\\ &+b_{(j+1)5}g^2+b_{(j+1)6}gq_j+b_{(j+1)7}q_j^2+b_{(j+1)8}g^2q_j\\ &+b_{(j+1)9}gq_j^2+b_{(j+1)10}q_j^3=0, \end{aligned} \tag{53}$$

where the coefficients presented in Eqs. (52) and (53) are provided in Appendix B.

In the following analysis, the method of multiple time scales is employed to solve the ODEs. First, a small but finite book keeping parameter ε and new independent time variables $T_0=\varepsilon^0\tau$, $T_2=\varepsilon^2\tau$ are introduced. In order to balance the damping, excitation and nonlinear terms, μ_a, b_{13}, b_{110}, μ_{cj}, $b_{(j+1)1}$, $b_{(j+1)2}$ and $b_{(j+1)m}$ (m = 8, 9, 10) are replaced with $\varepsilon^2\overline{\mu}_a$, $\varepsilon^2\overline{b}_{13}$, $\varepsilon^2\overline{b}_{110}$, $\varepsilon^2\overline{\mu}_{cj}$, $\varepsilon^2\overline{b}_{(j+1)1}$, $\varepsilon^2\overline{b}_{(j+1)2}$ and $\varepsilon^2\overline{b}_{(j+1)m}$, respectively. b_{12}, b_{1n} (n = 4, 5,…, 9), $b_{(j+1)3}$ and $b_{(j+1)(m-3)}$ are replaced with $\varepsilon\overline{b}_{12}$, $\varepsilon\overline{b}_{1n}(n$ = 4, 5,…9), $\varepsilon\overline{b}_{(j+1)3}$ and $\varepsilon\overline{b}_{(j+1)(m-3)}$, respectively. Then, by omitting the overbar, Eqs. (52) and (53) can be rewritten as:

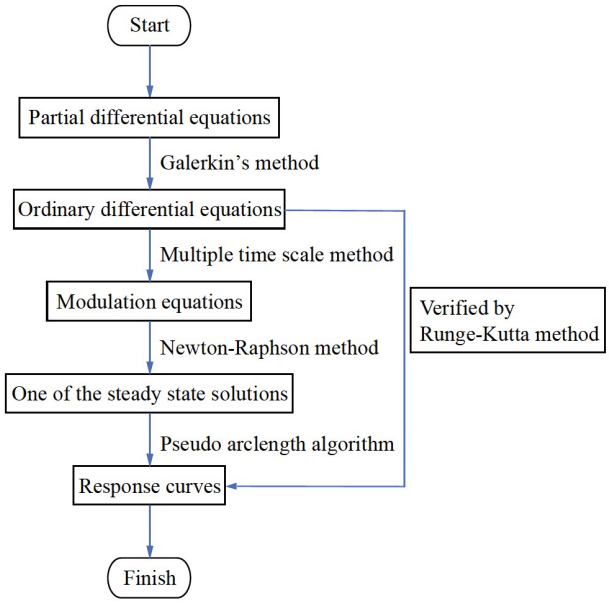

Figure 2 The flow chart of the solution process.

$$\begin{aligned} &g_{,\tau\tau}+\varepsilon^2\mu_a g_{,\tau}+\omega_a^2 g+\varepsilon b_{12}g^2+\varepsilon^2 b_{13}g^3+\varepsilon b_{14}q_1+\varepsilon b_{15}gq_1\\ &+\varepsilon b_{16}q_2+\varepsilon b_{17}gq_2+\varepsilon b_{18}q_1^2+\varepsilon b_{19}q_2^2\\ &+\varepsilon^2 b_{110}\cos(\Omega\tau)=0, \end{aligned} \tag{54}$$

$$\begin{aligned} &q_{j,\tau\tau}+\varepsilon^2\mu_{cj}q_{j,\tau}+\varepsilon^2 b_{(j+1)1}g_{,\tau}+\varepsilon^2 b_{(j+1)2}g_{,\tau\tau}+\varepsilon b_{(j+1)3}g\\ &+\omega_j^2 q_j+\varepsilon b_{(j+1)5}g^2+\varepsilon b_{(j+1)6}gq_j+\varepsilon b_{(j+1)7}q_j^2+\varepsilon^2 b_{(j+1)8}g^2q_j\\ &+\varepsilon^2 b_{(j+1)9}gq_j^2+\varepsilon^2 b_{(j+1)10}q_j^3=0, \end{aligned} \tag{55}$$

where j = 1, 2. $\omega_a^2=b_{11}, \omega_1^2=b_{24}, \omega_2^2=b_{34}$ and they represent natural frequencies of the SA and two cables, respectively. To apply a second order approximation, the solutions of g and q_j are uniformly expanded in power series of ε as:

$$\begin{aligned} g&=\sum_{i=1}^{3}\varepsilon^{i-1}g_i(T_0,T_2)+O(\varepsilon^3),\\ q_j&=\sum_{i=1}^{3}\varepsilon^{i-1}q_{ji}(T_0,T_2)+O(\varepsilon^3), \end{aligned} \tag{56}$$

where, T_0 is the fast time scale and T_2 is the slow time scale. Substituting Eq. (56) into Eqs. (54) and (55) and equating the terms of like order in ε yield

$$\begin{aligned} &\varepsilon^0: (D_0^2+\omega_a^2)g_1=0,\\ &(D_0^2+\omega_j^2)q_{j1}=0, \end{aligned} \tag{57}$$

$$\begin{aligned}&\varepsilon^1:(D_0^2+\omega_a^2)g_2=-(b_{12}g_1^2+b_{14}q_{11}+b_{15}g_1q_{11}+b_{16}q_{21}+b_{17}g_1q_{21}+b_{18}q_{11}^2+b_{19}q_{21}^2),\\&(D_0^2+\omega_j^2)q_{j2}=-(b_{(j+1)3}g_1+b_{(j+1)5}g_1^2+b_{(j+1)6}g_1q_{j1}+b_{(j+1)7}q_{j1}^2),\end{aligned}\tag{58}$$

$$\begin{aligned}&\varepsilon^2:(D_0^2+\omega_a^2)g_3=-\big[\mu_aD_0^1g_1+2D_0^1D_2^1g_1+2b_{12}g_1g_2+b_{13}g_1^3+b_{14}q_{12}+b_{15}g_1q_{12}+b_{15}g_2q_{11}+b_{16}q_{22}\\&+b_{17}g_1q_{22}+b_{17}g_2q_{21}+2b_{18}q_{11}q_{12}+2b_{19}q_{21}q_{22}+b_{110}\cos(\Omega T_0)\big],\\&(D_0^2+\omega_j^2)q_{j3}=-(b_{(j+1)1}D_0^1g_1+b_{(j+1)2}D_0^2g_1+\mu_{cj}D_0^1q_{j1}+2D_0^1D_2^1q_{j1}+b_{(j+1)3}g_2+2b_{(j+1)5}g_1g_2\\&+b_{(j+1)6}g_1q_{j2}+b_{(j+1)6}g_2q_{j1}+2b_{(j+1)7}q_{j1}q_{j2}+b_{(j+1)8}g_1^2q_{j1}+b_{(j+1)9}g_1q_{j1}^2+b_{(j+1)10}q_{j1}^3),\end{aligned}\tag{59}$$

where D_n^m is a differential operator and it is defined as $D_n^m=\partial^m/\partial T_n(m=1,2$ and $n=0,2)$.

The solutions to Eq. (57) are well-known and they can be expressed as:

$$g_1=A_1(T_2)\exp(\mathrm{i}\omega_aT_0)+cc,\tag{60}$$

$$q_{j1}=A_{j+1}(T_2)\exp(\mathrm{i}\omega_jT_0)+cc,\tag{61}$$

where $A_m(T_2)(m=1,2,3)$ are complex-valued amplitudes of the modes and will be determined by imposing the solvability conditions. *cc* denotes the complex conjugate of the preceding terms at the right hand. As time goes on, the homogeneous solutions of Eq. (58) will disappear, leaving only the particular solutions. By substituting Eqs. (60) and (61) into Eq. (58), the solutions for Eq. (58) can be obtained. This paper focuses on one-to-one-to-one internal resonance among the modes of the SA and two cables when primary resonance of the SA occurs. Hence, substituting the solutions for Eq. (58) and Eqs. (60) and (61) into Eq. (59) yields

$$\begin{aligned}(D_0^2+\omega_a^2)g_3=&-\frac{1}{2}b_{110}\exp(\mathrm{i}T_0\Omega)-\mathrm{i}\exp(\mathrm{i}T_0\omega_a)\mu_a\omega_aA_1-2\mathrm{i}\exp(\mathrm{i}T_0\omega_a)\omega_aD_2^1A_1+\exp(\mathrm{i}T_0\omega_a)\Gamma_{11}A_1\\&+\exp(\mathrm{i}T_0\omega_a)\Gamma_{12}A_1^2B_1+\exp(\mathrm{i}T_0\omega_1)\Gamma_{13}A_1A_2B_1+\exp\big[\mathrm{i}T_0(2\omega_1-\omega_a)\big]\Gamma_{14}A_2^2B_1\\&+\exp(\mathrm{i}T_0\omega_2)\Gamma_{15}A_1A_3B_1+\exp\big[\mathrm{i}T_0(\omega_1+\omega_2-\omega_a)\big]\Gamma_{16}A_2A_3B_1+\exp\big[\mathrm{i}T_0(2\omega_2-\omega_a)\big]\Gamma_{17}A_3^2B_1\\&+\exp\big[\mathrm{i}T_0(2\omega_a-\omega_1)\big]\Gamma_{18}A_1^2B_2+\exp(\mathrm{i}T_0\omega_a)\Gamma_{19}A_1A_2B_2+\exp(\mathrm{i}T_0\omega_1)\Gamma_{110}A_2^2B_2\\&+\exp\big[\mathrm{i}T_0(\omega_a-\omega_1+\omega_2)\big]\Gamma_{111}A_1A_3B_2+\exp(\mathrm{i}T_0\omega_2)\Gamma_{112}A_2A_3B_2\\&+\exp\big[\mathrm{i}T_0(2\omega_2-\omega_1)\big]\Gamma_{113}A_3^2B_2+\exp\big[\mathrm{i}T_0(2\omega_a-\omega_2)\big]\Gamma_{114}A_1^2B_3\\&+\exp\big[\mathrm{i}T_0(\omega_a+\omega_1-\omega_2)\big]\Gamma_{115}A_1A_2B_3+\exp\big[\mathrm{i}T_0(2\omega_1-\omega_2)\big]\Gamma_{116}A_2^2B_3\\&+\exp(\mathrm{i}T_0\omega_a)\Gamma_{117}A_1A_3B_3+\exp(\mathrm{i}T_0\omega_1)\Gamma_{118}A_2A_3B_3+\exp(\mathrm{i}T_0\omega_2)\Gamma_{119}A_3^2B_3+\mathrm{NST}_1+cc,\end{aligned}\tag{62}$$

$$\begin{aligned}(D_0^2+\omega_j^2)q_{j3}=&-\mathrm{i}\exp(\mathrm{i}T_0\omega_j)\mu_{cj}\omega_jA_{j+1}-2\mathrm{i}\exp(\mathrm{i}T_0\omega_j)\omega_jD_2^1A_{j+1}-\mathrm{i}b_{(j+1)1}\exp(\mathrm{i}T_0\omega_a)\omega_aA_1\\&+\exp(\mathrm{i}T_0\omega_a)\Gamma_{(j+1)1}A_1+\exp(\mathrm{i}T_0\omega_j)\Gamma_{(j+1)2}A_{j+1}+\exp(\mathrm{i}T_0\omega_{j+1})\Gamma_{(j+1)3}A_{j+2}\\&+\exp(\mathrm{i}T_0\omega_a)\Gamma_{(j+1)4}A_1^2B_1+\exp(\mathrm{i}T_0\omega_j)\Gamma_{(j+1)5}A_1A_{j+1}B_1\\&+\exp\big[\mathrm{i}T_0(2\omega_j-\omega_a)\big]\Gamma_{(j+1)6}A_{j+1}^2B_1+\exp(\mathrm{i}T_0\omega_{j+1})\Gamma_{(j+1)7}A_1A_{j+2}B_1\\&+\exp\big[\mathrm{i}T_0(\omega_j+\omega_{j+1}-\omega_a)\big]\Gamma_{(j+1)8}A_{j+1}A_{j+2}B_1+\exp\big[\mathrm{i}T_0(2\omega_{j+1}-\omega_a)\big]\Gamma_{(j+1)9}A_{j+2}^2B_1\\&+\exp\big[\mathrm{i}T_0(2\omega_a-\omega_j)\big]\Gamma_{(j+1)10}A_1^2B_{j+1}+\exp(\mathrm{i}T_0\omega_a)\Gamma_{(j+1)11}A_1A_{j+1}B_{j+1}\\&+\exp(\mathrm{i}T_0\omega_j)\Gamma_{(j+1)12}A_{j+1}^2B_{j+1}+\exp\big[\mathrm{i}T_0(\omega_a-\omega_j+\omega_{j+1})\big]\Gamma_{(j+1)13}A_1A_{j+2}B_{j+1}\\&+\exp\big[\mathrm{i}T_0(2\omega_{j+1}-\omega_j)\big]\Gamma_{(j+1)14}A_{j+2}^2B_{j+1}+\exp\big[\mathrm{i}T_0(2\omega_a-\omega_{j+1})\big]\Gamma_{(j+1)15}A_1^2B_{j+2}\\&+\exp\big[\mathrm{i}T_0(\omega_a+\omega_j-\omega_{j+1})\big]\Gamma_{(j+1)16}A_1A_{j+1}B_{j+2}+\exp(\mathrm{i}T_0\omega_a)\Gamma_{(j+1)17}A_1A_{j+2}B_{j+2}\\&+\exp(\mathrm{i}T_0\omega_j)\Gamma_{(j+1)18}A_{j+1}A_{j+2}B_{j+2}+\mathrm{NST}_{j+1}+cc,\end{aligned}\tag{63}$$

where $B_m(T_2)$ denote the complex conjugates of $A_m(T_2)$ and $j = 1, 2$. It should be noted that when $j = 2$, $j + 2$ should be set as 2 and ω_{j+1} should be set as ω_1. NST_m represents non-secular terms and Γ_{mn}(m = 1, 2, 3; n = 1, 2, …, 19) are provided in Appendix C. The external and internal resonance conditions are controlled by the detuning parameters σ,σ_1 and σ_2, namely

$$\Omega = \omega_a + \varepsilon^2\sigma,\ \omega_1 = \omega_a + \varepsilon^2\sigma_1,\ \omega_2 = \omega_a + \varepsilon^2\sigma_2. \tag{64}$$

The polar form of $A_m(T_2)$ (m = 1,2,3) can be expressed as:

$$A_m(T_2) = \frac{1}{2}a_m(T_2)\exp\left[\mathrm{i}\Phi_m(T_2)\right], \tag{65}$$

where a_m and Φ_m are the amplitude and phase angle of A_m, respectively. By substituting Eq. (65) into Eqs. (62) and (63) and separating the real and imaginary parts, the autonomous modulation equations in the polar form can be obtained as:

$$\begin{aligned}8\omega_a a_{1,\tau} =& -4\mu_a\omega_a a_1 - 4b_{110}\sin\alpha_1 + \Gamma_{110}a_2^3\sin\alpha_2 + a_1^2a_2\sin\alpha_2(\Gamma_{13}-\Gamma_{18}) + \Gamma_{14}a_1a_2^2\sin(2\alpha_2)\\ &+a_2a_3^2[\Gamma_{118}\sin\alpha_2 - \Gamma_{113}\sin(\alpha_2-2\alpha_3)] + \Gamma_{119}a_3^3\sin\alpha_3 + a_2^2a_3[\Gamma_{116}\sin(2\alpha_2-\alpha_3)\\ &+\Gamma_{112}\sin\alpha_3] + a_1^2a_3\sin\alpha_3(\Gamma_{15}-\Gamma_{114}) + \Gamma_{17}a_1a_3^2\sin(2\alpha_3) + a_1a_2a_3[\Gamma_{115}\sin(\alpha_2-\alpha_3)\\ &+\Gamma_{16}\sin(\alpha_2+\alpha_3) - \Gamma_{111}\sin(\alpha_2-\alpha_3)],\end{aligned} \tag{66}$$

$$\begin{aligned}8\omega_a a_1\alpha_{1,\tau} =& (4\Gamma_{11}+8\sigma\omega_a)a_1 + \Gamma_{12}a_1^3 - 4b_{110}\cos\alpha_1 + \Gamma_{110}a_2^3\cos\alpha_2 + a_1^2a_2\cos\alpha_2(\Gamma_{13}+\Gamma_{18})\\ &+a_1a_2^2[\Gamma_{19}+\Gamma_{14}\cos(2\alpha_2)] + a_2a_3^2[\Gamma_{118}\cos\alpha_2 + \Gamma_{113}\cos(\alpha_2-2\alpha_3)] + \Gamma_{119}a_3^3\cos\alpha_3\\ &+a_1a_3^2[\Gamma_{117}+\Gamma_{17}\cos(2\alpha_3)] + a_1a_2a_3\cos(\alpha_2-\alpha_3)(\Gamma_{111}+\Gamma_{115}) + a_1a_2a_3\Gamma_{16}\cos(\alpha_2+\alpha_3)\\ &+a_2^2a_3[\Gamma_{116}\cos(2\alpha_2-\alpha_3) + \Gamma_{112}\cos(\alpha_3)] + a_1^2a_3(\Gamma_{114}+\Gamma_{15})\cos\alpha_3,\end{aligned} \tag{67}$$

$$\begin{aligned}8\omega_j a_{j+1,\tau} =& -4\mu_{cj}\omega_j a_{j+1} - \Gamma_{(j+1)4}a_1^3\sin\alpha_{j+1} - a_1(4b_{(j+1)1}\omega_a\cos\alpha_{j+1} + 4\Gamma_{(j+1)1}\sin\alpha_{j+1})\\ &+a_1a_{j+1}^2\sin\alpha_{j+1}(\Gamma_{(j+1)6}-\Gamma_{(j+1)11}) - \Gamma_{(j+1)10}a_1^2a_{j+1}\sin(2\alpha_{j+1}) - 4\Gamma_{(j+1)3}a_{j+2}\sin(\alpha_{j+1}-\alpha_{j+2})\\ &-a_1a_{j+2}^2\left[\Gamma_{(j+1)17}\sin\alpha_{j+1} + \Gamma_{(j+1)9}\sin(\alpha_{j+1}-2\alpha_{j+2})\right] - \Gamma_{(j+1)14}a_{j+1}a_{j+2}^2\sin(2\alpha_{j+1}-2\alpha_{j+2})\\ &-a_1^2a_{j+2}\left[\Gamma_{(j+1)7}\sin(\alpha_{j+1}-\alpha_{j+2}) + \Gamma_{(j+1)15}\sin(\alpha_{j+1}+\alpha_{j+2})\right] + a_1a_{j+1}a_{j+2}\Gamma_{(j+1)8}\sin\alpha_{j+2}\\ &-a_1a_{j+1}a_{j+2}\left[\Gamma_{(j+1)13}\sin(2\alpha_{j+1}-\alpha_{j+2}) + \Gamma_{(j+1)16}\sin\alpha_{j+2}\right],\end{aligned} \tag{68}$$

$$\begin{aligned}8\omega_a\omega_1 a_1a_2\alpha_{2,\tau} =& (4\Gamma_{11}\omega_1 - 4\Gamma_{22}\omega_a + 8\sigma_1\omega_a\omega_1)a_1a_2 - 4b_{110}\omega_1a_2\cos\alpha_1 - \Gamma_{24}\omega_a a_1^4\cos\alpha_2\\ &+a_1^2a_2^2(\Gamma_{13}\omega_1\cos\alpha_2 + \Gamma_{18}\omega_1\cos\alpha_2 - \Gamma_{211}\omega_a\cos\alpha_2 - \Gamma_{26}\omega_a\cos\alpha_2)\\ &+\Gamma_{110}\omega_1a_2^4\cos\alpha_2 + a_1^3a_2[\Gamma_{12}\omega_1 - \Gamma_{25}\omega_a - \Gamma_{210}\omega_a\cos(2\alpha_2)]\\ &+a_1a_2^3[\Gamma_{19}\omega_1 - \Gamma_{212}\omega_a + \Gamma_{14}\omega_1\cos(2\alpha_2)] + \Gamma_{119}\omega_1a_2a_3^3\cos\alpha_3\\ &-a_1^2a_3^2[\Gamma_{217}\omega_a\cos\alpha_2 + \Gamma_{29}\omega_a\cos(\alpha_2-2\alpha_3)] - a_1^3a_3\{\Gamma_{27}\omega_a\cos(\alpha_2-\alpha_3)\\ &+a_2^2a_3^2[\Gamma_{118}\omega_1\cos\alpha_2 + \Gamma_{113}\omega_1\cos(\alpha_2-2\alpha_3)] + \Gamma_{215}\omega_a\cos(\alpha_2+\alpha_3)\}\\ &-4\Gamma_{23}\omega_a a_1a_3\cos(\alpha_2-\alpha_3) + a_2^3a_3[\Gamma_{116}\omega_1\cos(2\alpha_2-\alpha_3) + \Gamma_{112}\omega_1\cos\alpha_3]\\ &+a_1^2a_2a_3[\Gamma_{15}\omega_1\cos\alpha_3 - \Gamma_{213}\omega_a\cos(2\alpha_2-\alpha_3)] + a_1^2(4b_{21}\omega_a^2\sin\alpha_2 - 4\Gamma_{21}\omega_a\cos\alpha_2)\\ &+a_1^2a_2a_3(\Gamma_{114}\omega_1\cos\alpha_3 - \Gamma_{216}\omega_a\cos\alpha_3 - \Gamma_{28}\omega_a\cos\alpha_3)\\ &+a_1a_2a_3^2[\Gamma_{17}\omega_1\cos2\alpha_3 - \Gamma_{218}\omega_a + \Gamma_{117}\omega_1 - \Gamma_{214}\omega_a\cos(2\alpha_2-2\alpha_3)]\\ &+a_1a_2^2a_3[\Gamma_{111}\omega_1\cos(\alpha_2-\alpha_3) + \Gamma_{115}\omega_1\cos(\alpha_2-\alpha_3) + \Gamma_{16}\omega_1\cos(\alpha_2+\alpha_3)],\end{aligned} \tag{69}$$

$$
\begin{aligned}
8\omega_a\omega_2 a_1 a_3 \alpha_{3,\tau} = {} & (4\Gamma_{11}\omega_2 - 4\Gamma_{32}\omega_a + 8\sigma_2\omega_a\omega_2)a_1 a_3 - 4b_{110}\omega_2 a_3 \cos\alpha_1 - \Gamma_{34}\omega_a a_1^4 \cos\alpha_3 \\
& + a_1^2 a_3^2(\Gamma_{114}\omega_2 \cos\alpha_3 + \Gamma_{15}\omega_2 \cos\alpha_3 - \Gamma_{311}\omega_a \cos\alpha_3 - \Gamma_{36}\omega_a \cos\alpha_3) \\
& + \Gamma_{119}\omega_2 a_3^4 \cos\alpha_3 + a_1^3 a_3[\Gamma_{12}\omega_2 - \Gamma_{35}\omega_a - \Gamma_{310}\omega_a \cos(2\alpha_3)] \\
& + a_1 a_3^3[\Gamma_{117}\omega_2 - \Gamma_{312}\omega_a + \Gamma_{17}\omega_2 \cos(2\alpha_3)] + \Gamma_{110}\omega_2 a_3 a_2^3 \cos\alpha_2 \\
& - a_1^2 a_3^2[\Gamma_{317}\omega_a \cos\alpha_3 + \Gamma_{39}\omega_a \cos(2\alpha_2 - \alpha_3)] - a_1^3 a_2\{\Gamma_{37}\omega_a \cos(\alpha_2 - \alpha_3) \\
& + a_2^2 a_3^2[\Gamma_{112}\omega_2 \cos\alpha_2 + \Gamma_{116}\omega_2 \cos(2\alpha_2 - \alpha_3)] + \Gamma_{315}\omega_a \cos(\alpha_2 + \alpha_3)\} \\
& - 4\Gamma_{33}\omega_a a_1 a_2 \cos(\alpha_2 - \alpha_3) + a_3^3 a_2(\Gamma_{113}\omega_2 \cos(\alpha_2 - 2\alpha_3) + \Gamma_{118}\omega_2 \cos\alpha_2) \\
& + a_1^2 a_2 a_3[\Gamma_{18}\omega_2 \cos\alpha_2 - \Gamma_{313}\omega_a \cos(\alpha_2 - 2\alpha_3)] + a_1^2(4b_{31}\omega_a^2 \sin\alpha_3 - 4\Gamma_{31}\omega_a \cos\alpha_3) \\
& + a_1^2 a_2 a_3(\Gamma_{13}\omega_2 \cos\alpha_2 - \Gamma_{316}\omega_a \cos\alpha_2 - \Gamma_{38}\omega_a \cos\alpha_2) \\
& + a_1 a_2 a_3^2[\Gamma_{14}\omega_2 \cos 2\alpha_2 - \Gamma_{318}\omega_1 + \Gamma_{19}\omega_2 - \Gamma_{314}\omega_a \cos(2\alpha_2 - 2\alpha_3)] \\
& + a_1 a_2^2 a_3[\Gamma_{111}\omega_2 \cos(\alpha_2 - \alpha_3) + \Gamma_{115}\omega_2 \cos(\alpha_2 - \alpha_3) + \Gamma_{16}\omega_2 \cos(\alpha_2 + \alpha_3)],
\end{aligned} \tag{70}
$$

where

$$\alpha_1 = \sigma T_2 - \Phi_1, \quad \alpha_2 = \sigma_1 T_2 - \Phi_1 + \Phi_2, \quad \alpha_3 = \sigma_2 T_2 - \Phi_1 + \Phi_3.$$

The steady-state equilibrium solutions of Eqs. (66)-(70) can be determined by letting $a_{1,\tau} = a_{2,\tau} = a_{3,\tau} = \alpha_{1,\tau} = \alpha_{2,\tau} = \alpha_{3,\tau} = 0$. Using the Newton-Raphson method, one of the equilibrium solutions can be obtained. Starting with the point obtained by the Newton-Raphson method, the frequency-/force-response curves are extracted through the pseudo arc-length algorithm [37]. The stability of the equilibrium solutions can be checked by evaluating whether the real part of each eigenvalue is negative or not [38]. Due to the complexity caused by the nonlinearity, the allowable solutions of the system may be many; however, only typical solutions are discussed in this study.

4. Numerical results and discussion

In this section, based on the obtained theoretical solutions, the dynamic behaviors of a cable-stayed bridge are presented and discussed. A bridge model shown in Fig. 1 is considered here. It is symmetrical and the two cables are exactly identical with the length of $l_c = 200$ m. The total length of the SA is $L = 300$ m, and the lengths of each SA segment are 90 m, 120 m and 90 m, respectively. The physical parameters are as follows. For the cables: mass per unit length $m_c = 48.62$ kg/m, cross-sectional area $A_c = 7.8\times10^{-3}$ m^2, Young's modulus $E_c = 2.1\times10^{11}$ Pa, initial force of the cable $H_c = 4$ MN, and acute angle between the cable and the horizontal axis $\theta_1 = \theta_2 = \pi/6$. For the SA: mass per unit length $m_a = 16877$ kg/m, cross-sectional area $A_a = 2.15$ m^2, Young's modulus $E_a = 2\times10^{11}$ Pa, and moment inertia of cross section $I_a = 1.2$ m^4. Based on the above parameters, the values of some key variables are given in Table 1. Moreover, the initial deflection of the SA is expressed as $y_a = f_a \sin(\pi s)$. f_a is non-dimensional rise of the SA, which is used to adjust the frequencies of global modes to satisfy various internal resonance relationships under different vertical stiffness. It can be seen from Eqs. (41) and (42) that k_1 and k_2 affect the modal (trial) functions through boundary conditions, thereby affecting the nonlinear behaviors of the model. Hence, in the following, a detailed analysis of the nonlinear phenomena will be conducted under the following three different combinations of k_1 and k_2: (1) Case 1: $k_1 = k_2 = 10^6$; (2) Case 2: $k_1 = k_2 = 10^4$; and (3) Case 3: $k_1 = 10^4$, $k_2 = 10^6$.

4.1 Case 1: nonlinear analysis when $k_1 = k_2 = 10^6$

In this section, the model with ideal boundaries (i.e., H-H ends) is simulated and its nonlinear behaviors are investigated. For the H-H ends, $k_1 = k_2 \to \infty$. Here, k_1 and k_2 are assumed to be 10^6 and the corresponding stiffness is 8.89×10^9 N/m. The circular frequencies of the SA and cables are 4.37 and 4.54, respectively. f_a is taken as 0.035 to satisfy the internal resonance relationship.

The frequency-response curves are obtained by the pseudo arc-length algorithm and presented in Fig. 3. In the following figures, SN, HB and PF denote saddle-node, Hopf and pitchfork bifurcations, respectively. Stable solutions are depicted by solid lines and unstable by dashed lines. In order to validate the obtained theoretical results, the Runge-Kutta method is also applied by integrating directly Eqs. (52) and (53). As illustrated in Fig. 3, the results obtained from the theoretical derivation are well aligned with the numerical simulation results. It should be noted that the higher amplitude values are not easy to obtain, as one needs to know their domains of attraction.

In Fig. 3a, the frequency-response curve of the SA bends to

Table 1 Key parameters of the SA and cables

SA		cables		
β_a	η	ψ_{cj}	λ_{cj}	β_{cj}
4.88531	161250	1.07839	409.5	0.69728

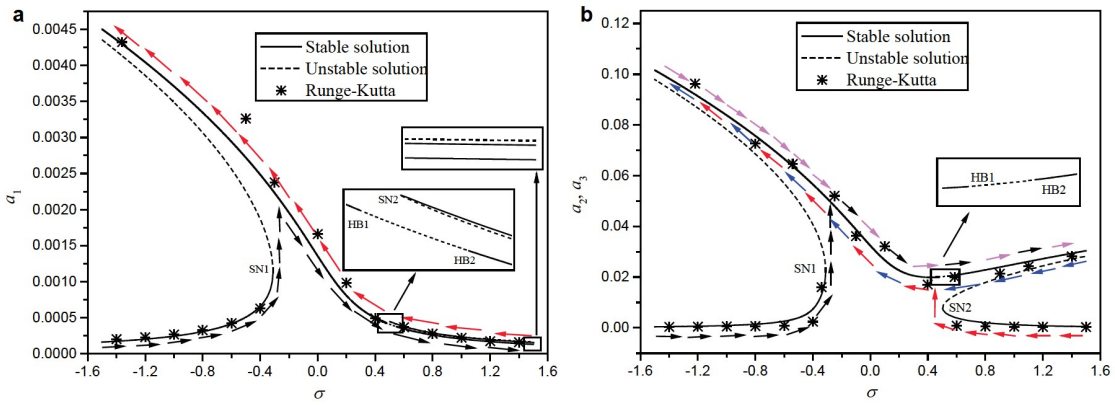

Figure 3 The frequency-response curves with excitation amplitude $F = 0.005$ and $\sigma_1 = \sigma_2 = 0.167$: **a** for SA and **b** for cables.

the left and exhibits as a softening spring characteristic, which leads to multivalued amplitudes. When σ increases from a relatively small value, the amplitude of the response increases slowly until SN1 is reached, where the tangent of the curve is vertical. At this moment, slowly increasing σ beyond SN1 will cause a sudden jump from the lower branch to the upper branch, which is the so-called jump phenomenon. After that, a_1 decreases with an increase in σ and loses its stability via HB1, while regaining stability at HB2. Different from a_1, a_2 (a_3) increases with an increase in σ after HB1. This may be because the SA transfers energy to cables due to the deck-cable modal interaction [39]. Conversely, as σ is reduced from a relatively large value, the jump phenomenon also takes place via SN2 (see Fig. 3b). From that point on, a_1, a_2 and a_3 increase gradually with a decrease in σ. By examining the curve carefully, it is found that there are no stable solutions in a small range between SN2 and HB1 (see the enlarged part in Fig. 3a), which means that if a frequency (i.e., σ)sweeping experiment is conducted, there is no way to find a stable solution within a small frequency interval. This may be related to the amount of energy that the model absorbs from the external excitation.

In Fig. 3b, there exist two peaks. One bends to the left and the other bends to the right. This is a double-jump phenomenon, which has also been observed in previous work [25,40]. Due to the double-jump phenomenon, the cables may vibrate with different amplitudes. That is to say, both of the amplitudes of the two cables belong to the upper branch or lower branch, depending on the initial conditions. Comparing Fig. 3a and b, it can be seen that the SA and cables exhibit different nonlinear behaviors at SN2. As σ is reduced from a relatively large value, a_1 jumps down to the lower branch from the upper branch, while a_2 (a_3) jumps up to the upper branch from the lower branch. This is consistent with the phenomenon observed in the Ref. [26]. In addition, an interesting phenomenon is observed in Fig. 3a. In the first half of the upper right branch, the stable solution is above the unstable solution, while in the second half, it is below the unstable solution, as illustrated in the enlarged parts in Fig. 3a. The reason may be that as σ is increased, the excitation frequency is far away from the primary resonance region, thereby making the amplitude of the SA drop sharply. In addition, the response amplitudes of cables are much greater than those of the SA, which is consistent with large vibrations of cables in practice. This is because the SA provides a forced and parametric excitation at the lower end of the cable. In this case, even small excitation amplitude will cause a large vibration of the cables. The above observations and discussion reveal, at least to some extent, the reason why the large vibrations of cables take place in a real-world bridge.

In order to explore the effects of the excitation on nonlinear behaviors of the model, the frequency-response curves with different excitation amplitudes are depicted, as illustrated in Fig. 4. It can be seen that the response amplitudes of the SA and cables increase with an increase in excitation amplitude. When σ falls into the interval of $[-0.6,0.6]$, the amplitudes increase obviously. However, when σ falls into the interval of $[-1.5,-0.6]$ and $[0.6,1.5]$, the increase in amplitudes is not so obvious and the lower branches of the cables are almost zero. The higher absolute value of σ corresponds to the lower possibility of the primary resonance. Therefore, the response amplitudes are not sensitive to the changes in excitation amplitudes. As shown in Fig. 4, the distance between two SNs (i.e., SN1 and SN2, SN3 and SN4, SN5 and SN6) becomes smaller as the excitation amplitude decreases. The SNs gradually shift to the lower right when $\sigma < 0$ and to the lower left when $\sigma > 0$. Moreover, the distance between two HBs (i.e., HB1 and HB2, HB3 and HB4) belonging to the same branch becomes smaller, and there are no HBs any more in the frequency-response curves when $F = 0.001$, as expected. Although HBs disappear, new branch point (PF1) appears (see Fig. 5), which is different from the phenomenon in the Ref. [26]. Due to the existence of PFs, there are as many as three stable solutions when $\sigma$is relatively large. It should be noted that the two stable branches of the SA caused by PF1 overlap. There are actually two stable

branches, which are very close to each other. It can be concluded that with the decrease in excitation amplitude, HBs will disappear but new branches take place and the nonlinear behaviors of the model become more complicated.

Keeping the excitation frequency (i.e., σ) fixed to a certain value and sweeping the excitation amplitude, the force-response curves are obtained, as presented in Figs. 6 and 7. It can be seen from Fig. 6 that the jump phenomenon triggered by SNs also occurs. When the value of F is relatively small, the lower branch increases with an increase in σ. However, when the value of F is relatively large, the upper branch decreases with an increase in σ, which is induced by softening spring characteristic. With the increase in σ, the range of unstable solutions between two SNs (i.e., SN1 and SN2, SN3 and SN4, SN5 and SN6) gradually narrows and the two SNs gradually shift to the lower left. When σ goes up to a certain value, say $\sigma = 0$, the two SNs are merged together and all the unstable solutions disappear, leaving only the stable solutions, as illustrated in Fig. 6. It is noted that the conditions leading to multivalued phenomenon are different. For $\sigma = -0.6$, as long as F is less than 0.014, multivalued phenomenon will occur and for $\sigma = -0.3$, it is 0.0047. However, for $\sigma = -0.1$, the value of F must be very small (less than 0.00068) in order for the multivalued phenomenon to take place. This indicates that when σ is less than zero, the increase in σ will make the multivalued phenomenon more difficult to occur. The above conclusions are in accordance with those in Fig. 4, and they can be mutually correlated with each other.

Figure 7 presents the force-response curves when $\sigma = 0.6$. As shown in Fig. 7b and d, the amplitudes of the cables are relatively small but still much larger than those of the SA. The branch exhibits a linear relationship between response and excitation amplitude, with no nonlinear characteristics. However, the other branches are relatively complicated, as illustrated in Fig. 7a and c. When F is reduced from a relatively large value, response amplitudes decrease correspondingly until PF is reached and three new branches are generated via PF, which is not found in the Ref. [26]. After PF, an interesting phenomenon can be observed. For the cables, as F decreases, one of the branches further decreases, losing its stability via SN1, and the stable solutions are below the unstable ones. Another branch loses its stability via SN2 and the stable solutions are above the unstable ones. Hence, for the SA, there are actually two almost identical branches

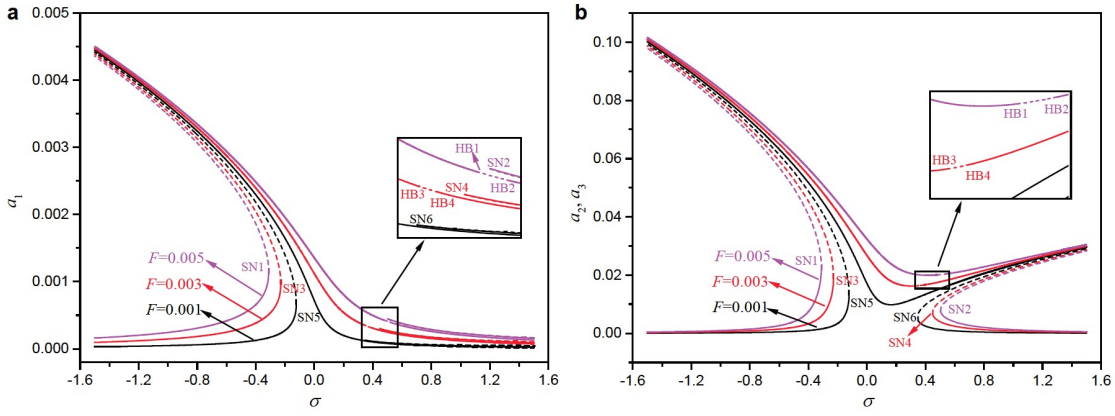

Figure 4 The frequency-response curves with different excitation amplitudes and $\sigma_1 = \sigma_2 = 0.167$: **a** for SA and **b** for cables.

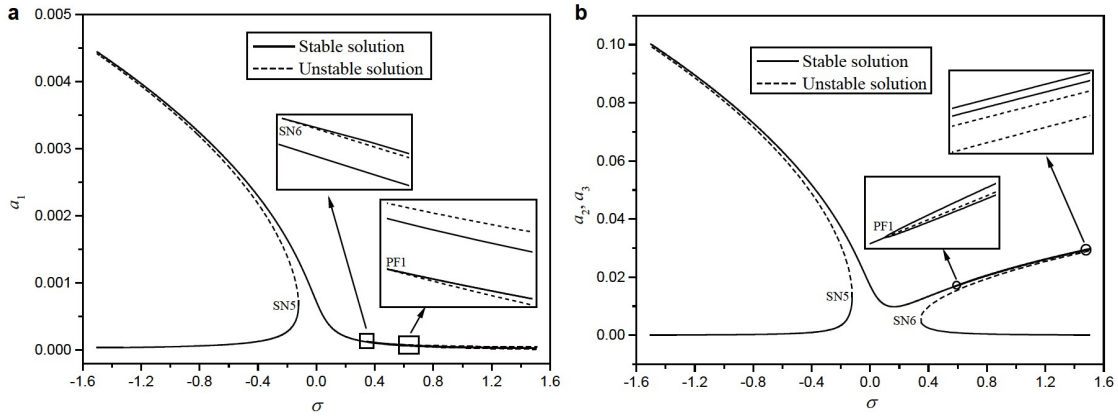

Figure 5 The frequency-response curves with excitation amplitude $F = 0.001$ and $\sigma_1 = \sigma_2 = 0.167$: **a** for SA and **b** for cables.

that overlap each other. The solutions of third branch are all unstable, and SN3 does not change their stability. After SN3, a_1 goes up to the upper right, and a_2 (a_3) goes down to the lower right. The above phenomena may be induced by different vibration mechanisms. After all, there exist different terms in Eqs. (52) and (53). Furthermore, Fig. 7c once again reveals the multivalued phenomenon.

4.2 Case 2: nonlinear analysis when $k_1 = k_2 = 10^4$

This section presents the nonlinear behaviors of the model with moderate vertical stiffness. It is well-known that the bridge bearings are usually elastic and compressible to ensure a certain allowable displacement of the bridge. Generally, the vertical stiffness of the bearings is about in the magnitude order of 10^7. Hence, k_1 and k_2 are chosen to be in the magnitude of 10^4 and the corresponding stiffness is 8.89×10^7 N/m. The circular frequencies of the SA and cables are 4.49 and 4.54, respectively. f_a is taken as 0.048 to satisfy the internal resonance relationship.

In order to explore the effect of vertical stiffness on the nonlinear behaviors of the model, the frequency-response curves of the SA and cables with different vertical stiffness are presented, as illustrated in Fig. 8. It can be seen that due to the reduction in vertical stiffness, the response amplitudes decrease accordingly. It is because when $k_1 = k_2 = 10^4$, the

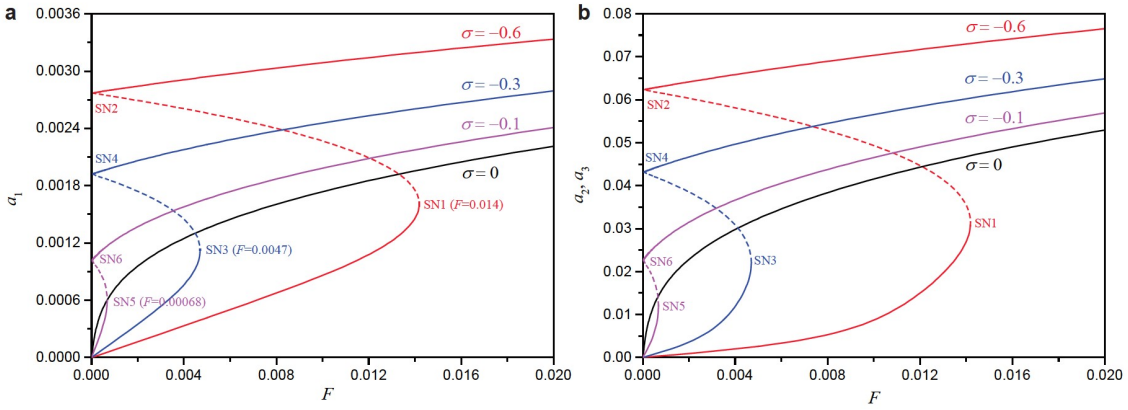

Figure 6 The force-response curves when $\sigma \leq 0$ and $\sigma_1 = \sigma_2 = 0.167$: **a** for SA and **b** for cables.

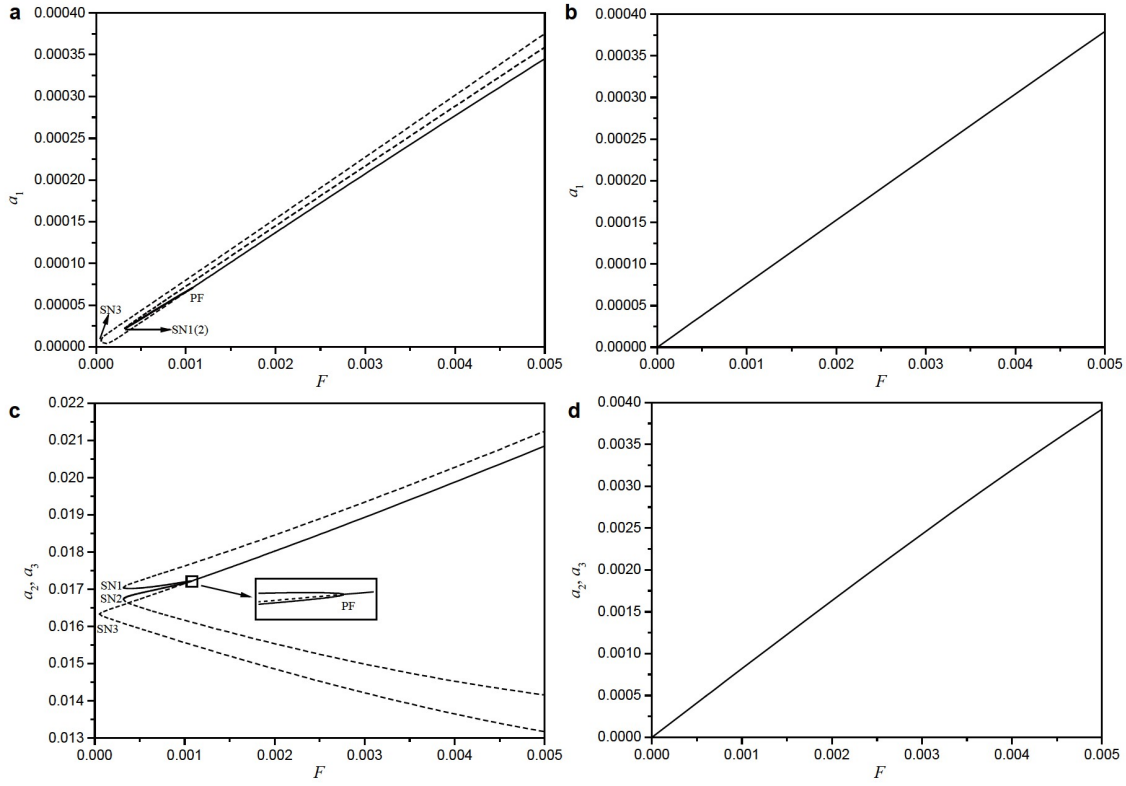

Figure 7 The force-response curves with $\sigma = 0.6$ and $\sigma_1 = \sigma_2 = 0.167$: **a**, **b** for SA and **c**, **d** for cables.

vertical elastic constraints dissipates a part of the energy, just like a spring. Obviously, the influence of vertical stiffness on the response amplitudes of cables is greater than that of the SA, which is interesting. This shows that the vertical stiffness has an important influence on the nonlinear behaviors of the cable. The reason may be that some of the energy that should be transferred to the cable is dissipated by the spring. In Fig. 8b, another interesting phenomenon is observed. The reduction of vertical stiffness does not work on the lower branches of the solution, but has a great impact on the upper branches, which is directly related to the large vibrations of the cables, and the nonlinear vibrations of the cables, as the key in the nonlinear dynamics of the cable-stayed bridge, should attract due attention. In addition, with the decrease in vertical stiffness, the frequency range between two SNs (i.e., SN1 and SN2, SN3 and SN4) narrows and HBs gradually move to the lower left. Simultaneously, new branch points occur (see the PF in Fig. 9). Recall that there is no PF in Fig. 3, which indicates that the reduction of vertical stiffness makes the nonlinear behaviors of the model more complex. However, in most cases, the boundary conditions are generally regarded as H-H end, which may ignore some important nonlinear phenomena.

Figure 10 presents the force-response curves with different vertical stiffness and σ. It shows that all the stable solutions in the case when $k_1 = k_2 = 10^4$ are smaller than those in the case when $k_1 = k_2 = 10^6$. The reason is the same as that in Fig. 8. The jump phenomenon takes place again and with the reduction of vertical stiffness, SN1 gradually moves outward, which means that for a given F, there may be multi-valued amplitudes when $k_1 = k_2 = 10^4$, but only a single amplitude when $k_1 = k_2 = 10^6$. Apparently, the response amplitudes of cables change more obviously, indicating that the vertical stiffness has a greater impact on the force-response of cables. The mass of cables is much smaller than that of the SA. Therefore, a slight change in energy will make a difference in the nonlinear behaviors of the cable. Figure 11 presents the force-response curves when σ= 0.6, from which a linear branch is also observed. With the decrease in vertical stiffness, the SNs and PFs gradually move to the upper right. Moreover, by comparing Fig. 11a and c, it is observed that the response amplitude when $k_1 = k_2 = 10^4$ is smaller than that when $k_1 = k_2 = 10^6$ (see Fig. 11a), while the conclusion is opposite in Fig. 11c, which is different from other figures. The reason may be that the cable gains more energy from SA to maintain its large vibration, although elastic constraints

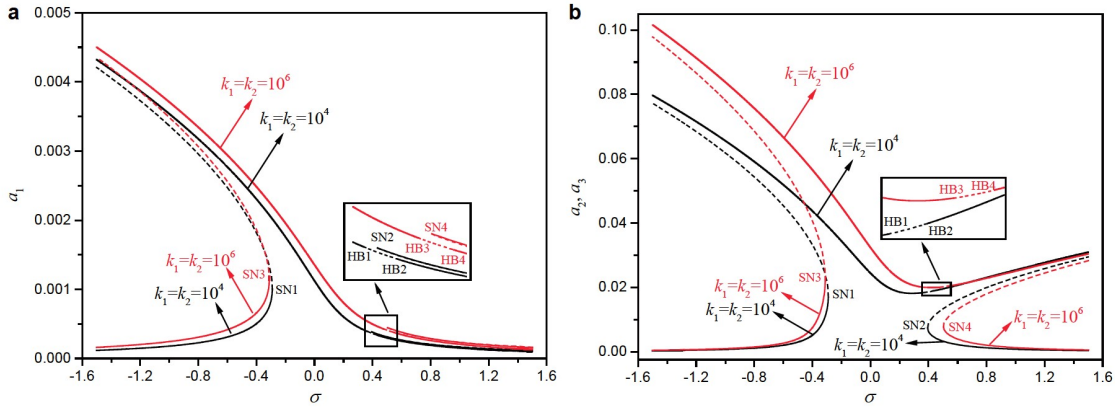

Figure 8 The frequency-response curves with different vertical stiffness when excitation amplitude F = 0.005: **a** for SA and **b** for cables.

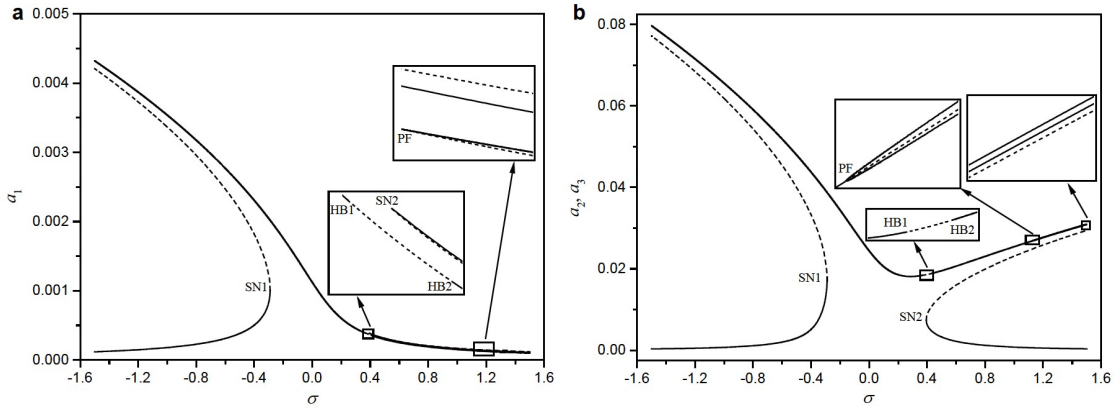

Figure 9 The frequency-response curves with $k_1 = k_2 = 10^4$ when excitation amplitude F = 0.005 and $\sigma_1 = \sigma_2$ = 0.051: **a** for SA and **b** for cables.

consume a part of the energy.

4.3 Case 3: nonlinear analysis when $k_1 = 10^4$ and $k_2 = 10^6$

In actual cable-stayed bridges, there may be some differences in the vertical stiffness of the bearings at both ends. In this case, the trial function of the SA exhibits asymmetrical characteristic and the internal resonance of the SA can be aroused [27]. Therefore, it is significant to study the nonlinear behaviors of the model with different stiffness at both ends. To this end, in this section, $k_1 = 10^4$ and $k_2 = 10^6$ are applied. The corresponding stiffness is 8.89×10^7 N/m and 8.89×10^9 N/m, respectively. The circular frequencies of the SA and cables are 4.40 and 4.54, respectively. f_a is taken as 0.04 to satisfy the internal resonance relationship.

Figure 12 presents the frequency-response curves of the SA and cables with different vertical stiffness. It should be noted that SNs and HBs are not marked in the diagram because they are not the focus of this section. It can be seen that the upper branches differ a lot compared with the cases where $k_1 = k_2 = 10^6$ and $k_1 = k_2 = 10^4$. The frequency-response curve of the SA experiences great growth, which indicates that more energy is allocated to the SA from the external

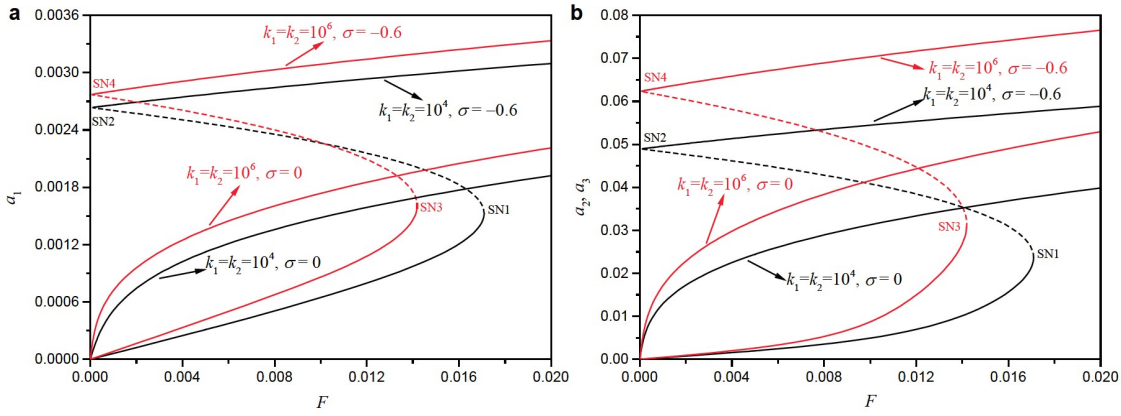

Figure 10 The force-response curves with different vertical stiffness when $\sigma \leq 0$: **a** for SA and **b** for cables.

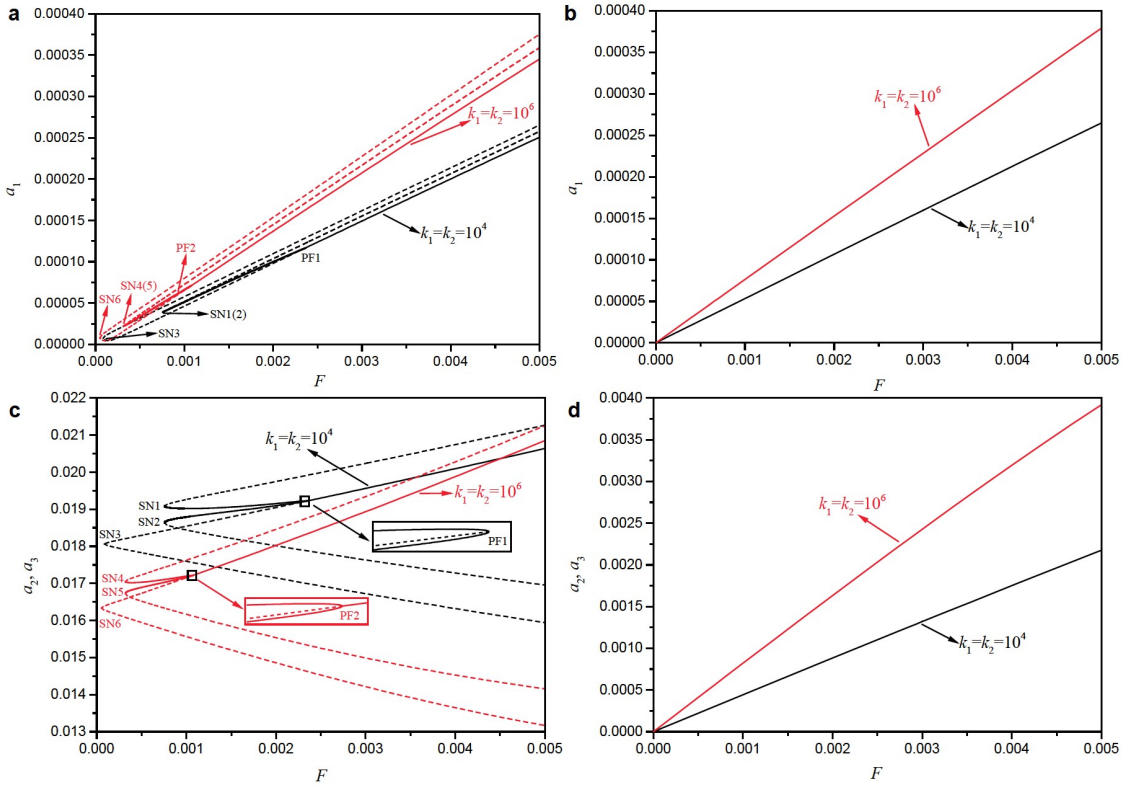

Figure 11 The force-response curves with different vertical stiffness when $\sigma = 0.6$: **a**, **b** for SA and **c**, **d** for cables.

excitation. Due to the different vertical stiffness at both ends, the structure is no longer symmetrical, and thus the frequency-response curves of the two cables are different. As shown in Fig. 12b, when $k_1 = 10^4$ and $k_2 = 10^6$, the upper branch of the frequency-response curve is between those of the other two curves, while it is the highest in Fig. 12c. The reason may be that the amount of energy transferred from the SA to the two cables is different and Cable 2 gains more energy. Or the energy is transferred between the two cables and Cable 1 transfers its energy to Cable 2 through the SA.

Figure 13 presents the frequency-response curves when $k_1 = 10^4$ and $k_2 = 10^6$ more clearly. In Fig. 13, no PF is observed, while new HBs occur and there are four HBs in total. For the lower branch when $\sigma > 0.4$, the stable solutions of a_2 are pretty close to the unstable solutions, which is different from a_3. The above phenomenon indicates that the difference in vertical stiffness at both ends leads to new nonlinear behaviors of the model.

Figure 14 presents the force-response curves with different vertical stiffness when $\sigma < 0$. Since the upper branches have been discussed in Fig. 12, only the lower branches will be discussed here. It can be seen from Fig. 14a that the amplitude in the case when $k_1 = 10^4$ and $k_2 = 10^6$ is the largest. However, as shown in Fig. 14b, the amplitude in the case when $k_1 = 10^4$ and $k_2 = 10^6$ is almost equal to that in the case when $k_1 = k_2 = 10^4$. In Fig. 14c, the amplitude in the case when $k_1 = 10^4$ and $k_2 = 10^6$ is between those in the other two cases (i.e., $k_1 = k_2 = 10^6$ and $k_1 = k_2 = 10^4$). The reason for the above phenomenon may be that the SA is allocated more energy and Cable 2 gains a medium amount of energy, being compared with the other two cases. However, Cable 1 does not gain extra energy compared with the case where $k_1 = k_2 = 10^4$. Figure 15 presents the force-response curves with different vertical stiffness when $\sigma = 0$. It shows that Fig. 15 and the upper branches in Fig. 14 are similar. Actually, they all correspond to the upper branches in Fig. 12.

Figure 16 presents the linear branches with different vertical stiffness when $\sigma = 0.6$. It can be observed that when $k_1 = 10^4$ and $k_2 = 10^6$, the amplitudes of both cables are all between those in the other two cases, which is different from Fig. 14. This reveals another way of energy transfer among the SA and cables. Figure 17 presents another branch with $k_1 = 10^4$ and $k_2 = 10^6$ when $\sigma = 0.6$. It shows that there are no PFs but SNs. Due to the disappearance of PFs, each graph in Fig. 17 has only one branch and the branches of which the solutions are all unstable disappear. Since the vertical stiffness on the side of Cable 1 is smaller ($k_1 = 10^4$), the elastic constraint will absorb a part of energy. Hence, compared with

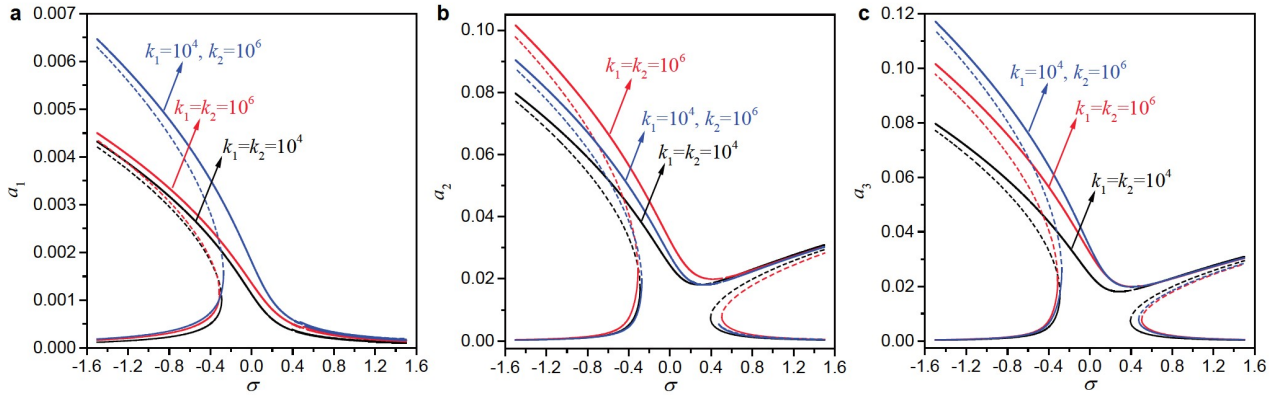

Figure 12 The frequency-response curves with different vertical stiffness when excitation amplitude $F = 0.005$: **a** for SA, **b** for cable 1 and **c** for cable 2.

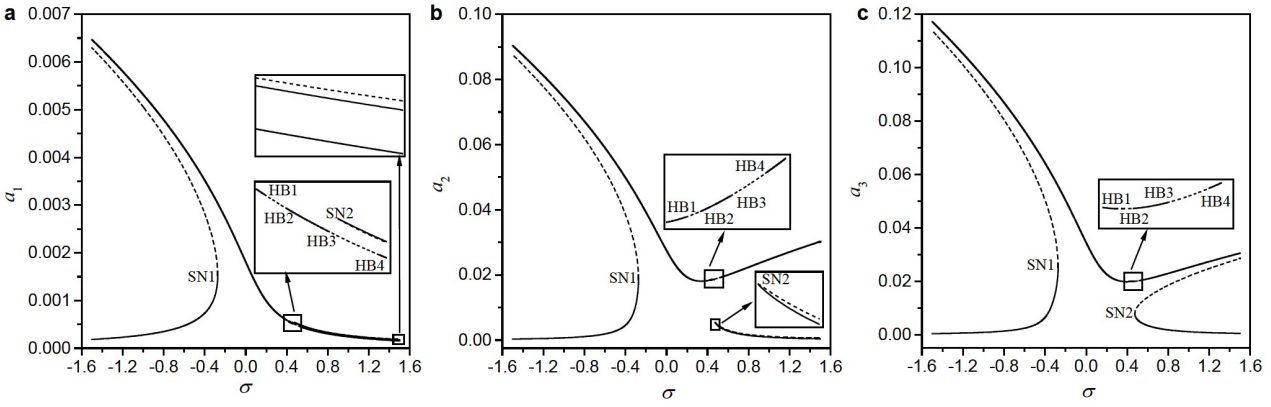

Figure 13 The frequency-response curves with $k_1 = 10^4$ and $k_2 = 10^6$ when excitation amplitude $F = 0.005$ and $\sigma_1 = \sigma_2 = 0.141$: **a** for SA, **b** for cable 1 and **c** for cable 2.

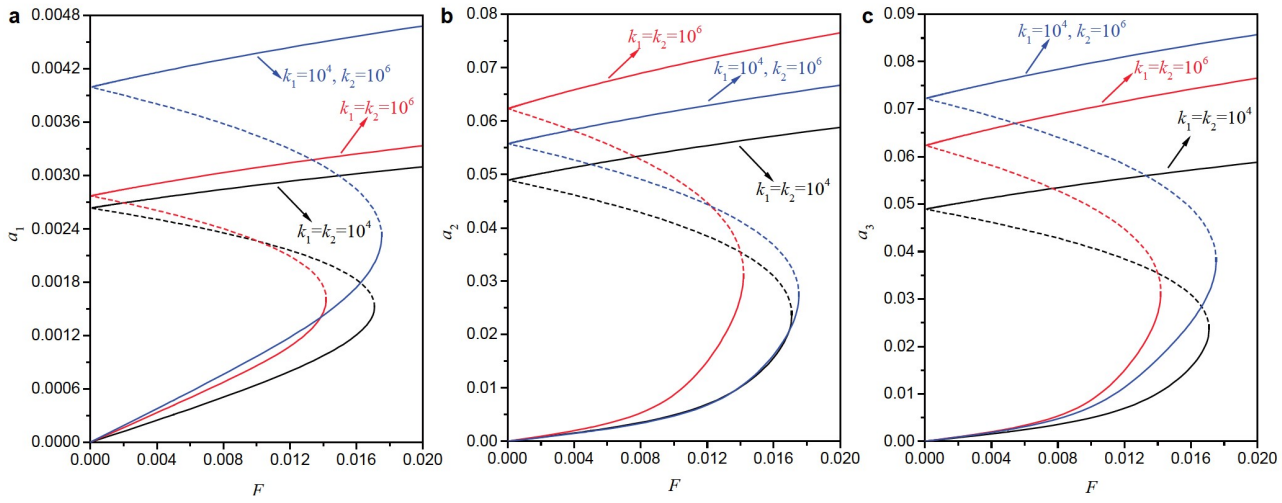

Figure 14 The force-response curves with different vertical stiffness when $\sigma = -0.6$: **a** for SA, **b** for cable 1 and **c** for cable 2.

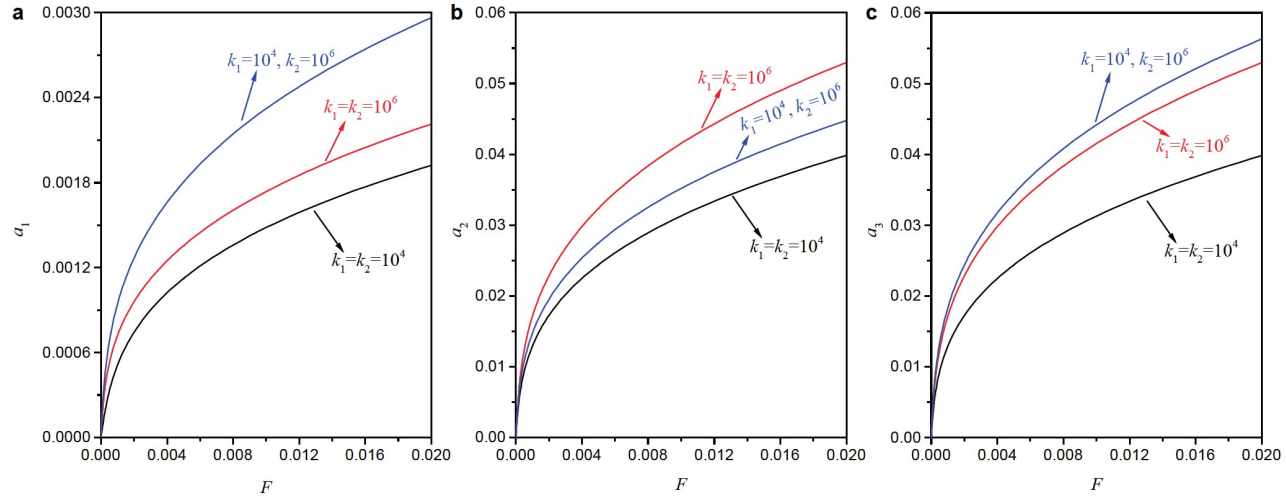

Figure 15 The force-response curves with different vertical stiffness when $\sigma = 0$: **a** for SA, **b** for cable 1 and **c** for cable 2.

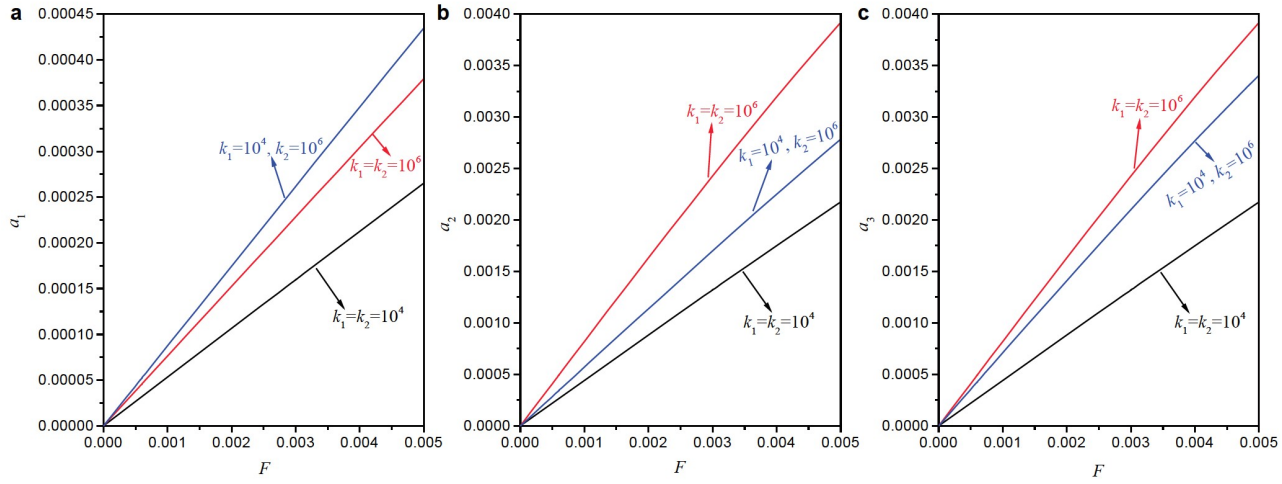

Figure 16 The force-response curves with different vertical stiffness when $\sigma = 0.6$: **a** for SA, **b** for cable 1 and **c** for cable 2.

the corresponding force-response curves in the other two cases, Cable 1 retains the lower branch (see Fig. 17b) and Cable 2 retains the upper branch (see Fig. 17c). This is induced by different boundary conditions and similar phe-

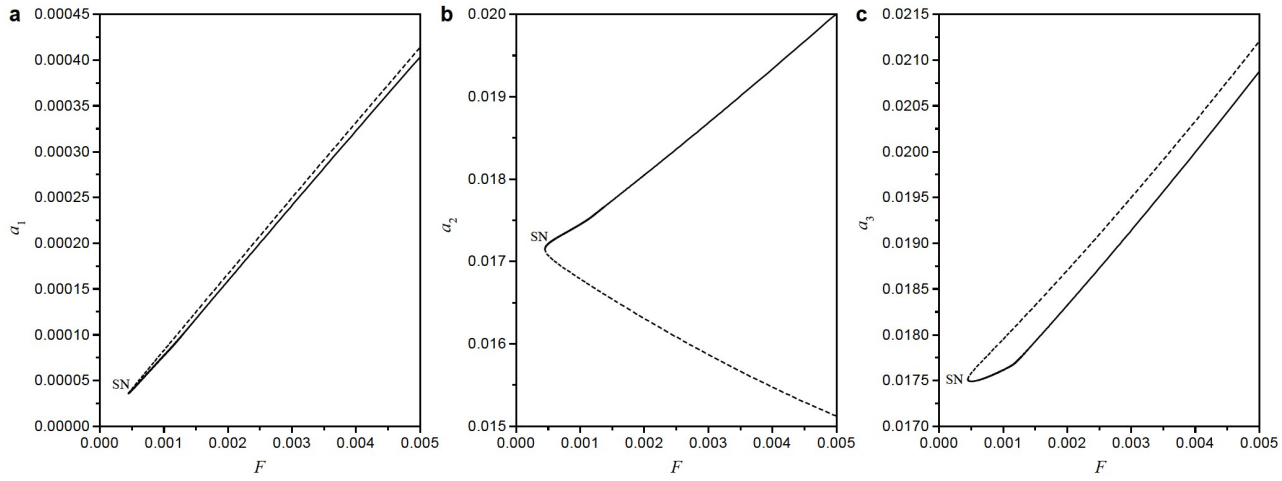

Figure 17 Another branch of the force-response curves with $k_1 = 10^4$ and $k_2 = 10^6$ when $\sigma = 0.6$ and $\sigma_1 = \sigma_2 = 0.141$; **a** for SA, **b** for cable 1, **c** for cable 2.

nomena are not observed in the Ref. [26].

5. Conclusions

In order to obtain the nonlinear dynamics of cable-stayed bridges more accurately, a double-cable-stayed shallow-arch model with elastic supports at both ends and the initial configuration of the bridge deck included in the modeling is developed in this study. The in-plane one-to-one-to-one internal resonance among global and local modes are studied when external primary resonance occurs. First, considering the boundary and continuous conditions, the separation-of-variable method is applied to solve the in-plane eigenvalue problem of the model. The obtained modal function is taken as the trial function of the SA and Galerkin's method is used to discrete differential equations of motion. In this way, a set of ODEs are derived. To solve the ODEs, the method of multiple time scales is utilized. Then, the stable equilibrium solutions of modulation equations are obtained by the Newton-Raphson method and the frequency-/force-response curves are extracted by the pseudo arc-length algorithm. In order to explore the influence of vertical stiffness on the dynamic behaviors of the system, the nonlinear analyses under three different combinations of k_1 and k_2 are carried out systematically. The following conclusions are drawn.

(1) The double-jump phenomenon is observed in the frequency-response curves of the cables. With the decrease in excitation amplitude, HBs disappear. However, new PFs are firstly observed in the frequency-force-response curves. Due to the existence of the PF, there are as many as three stable solutions when σ is relatively large. The SNs that do not separate stable equilibria from unstable equilibria are firstly observed in the force-response curves.

(2) The vertical stiffness has a greater influence on the cables, especially the large vibrations of the cables. Moreover, the vertical stiffness can change the nonlinear behaviors of the model, such as the numbers and types of bifurcations. Since a part of energy is dissipated by elastic constraints, the response amplitudes of the SA and cables decrease with the reduction of vertical stiffness.

(3) When the vertical stiffness at two ends is different, the frequency-force-response curves of the SA and cables are quite different from those in the other two cases. There is a redistribution of energy among the SA and cables. Overall, the asymmetry caused by the different stiffness makes the SA obtain more energy, while the nonlinear behaviors of the cables are more complicated. The energy obtained by the cables can be either large or small, depending on different energy transfer mechanisms.

(4) When the vertical stiffness at two ends is different, the PFs in the frequency-response curves disappear, but there are more HBs. Due to the disappearance of PFs, there is only one branch left in the force-response curve of Cable 1 (Cable 2) and Cable 1 retains the lower branch, while Cable 2 retains the upper branch. It suggests that the boundary conditions do have a significant influence on the nonlinear behaviors of the bridge system.

This work was supported by the National Natural Science Foundation of China (Grant Nos. 11972151 and 11872176).

1 C. Xing, H. Wang, A. Li, and Y. Xu, Study on wind-induced vibration control of a long-span cable-stayed bridge using TMD-type counterweight, J. Bridge Eng. **19**, 141 (2014).
2 N. Srinil, G. Rega, and S. Chucheepsakul, Large amplitude three-dimensional free vibrations of inclined sagged elastic cables, Nonlin. Dyn. **33**, 129 (2003).
3 X. Su, H. Kang, T. Guo, and Y. Cong, Modeling and parametric analysis of in-plane free vibration of a floating cable-stayed bridge with transfer matrix method, Int. J. Str. Stab. Dyn. **20**, 2050004 (2020).
4 Y. H. Zhao, and P. P. Zheng, Parameter analyses of suspended cables subjected to simultaneous combination, super and sub-harmonic excitations. Steel Compos. Struct. **40**, 203 (2021).
5 Y. Zhao, and H. Lin, Nonlinear dynamics of suspended cables under periodic excitation in thermal environments: two-to-one internal re-

sonance, Int. J. Bifurcat. Chaos **31**, 2150153 (2021).
6 Z. Zhang, H. Ding, Y. W. Zhang, and L. Q. Chen, Vibration suppression of an elastic beam with boundary inerter-enhanced nonlinear energy sinks, Acta Mech. Sin. **37**, 387 (2021).
7 Y. Zhao, and J. Du, Dynamic behavior analysis of an axially loaded beam supported by a nonlinear spring-mass system, Int. J. Str. Stab. Dyn. **21**, 2150152 (2021).
8 Y. Yang, H. Ding, and L. Q. Chen, Dynamic response to a moving load of a Timoshenko beam resting on a nonlinear viscoelastic foundation, Acta Mech. Sin. **29**, 718 (2013).
9 J. Su, K. Zhang, Q. Zhang, and Y. Tian, Free and forced vibration of coupled beam systems resting on variable viscoelastic foundations, Int. J. Str. Stab. Dyn. **20**, 2050141 (2020).
10 X. Geng, H. Ding, K. Wei, and L. Chen, Suppression of multiple modal resonances of a cantilever beam by an impact damper, Appl. Math. Mech.-Engl. Ed. **41**, 383 (2020).
11 Y. Zhao, Z. Wang, X. Zhang, and L. Chen, Effects of temperature variation on vibration of a cable-stayed beam, Int. J. Str. Stab. Dyn. **17**, 1750123 (2017).
12 Y. Fujino, P. Warnitchai, and B. M. Pacheco, An experimental and analytical study of autoparametric resonance in a 3DOF model of cable-stayed-beam. Nonlinear Dyn. **4**, 111 (1993).
13 V. Gattulli, and A. Paolone, Planar motion of a cable-supported beam with feedback controlled actions, J. Intel. Mater. Syst. Struct. **8**, 767 (1997).
14 V. Gattulli, M. Morandini, and A. Paolone, A parametric analytical model for non-linear dynamics in cable-stayed beam, Earthquake Engng. Struct. Dyn. **31**, 1281 (2002).
15 V. Gattulli, and M. Lepidi, Localization and veering in the dynamics of cable-stayed bridges, Comput. Struct. **85**, 1661 (2007).
16 E. Caetano, A. Cunha, and C. A. Taylor, Investigation of dynamic cable-deck interaction in a physical model of a cable-stayed bridge. Part I: Modal analysis, Earthquake Engng. Struct. Dyn. **29**, 481 (2000).
17 E. Caetano, A. Cunha, and C. A. Taylor, Investigation of dynamic cable-deck interaction in a physical model of a cable-stayed bridge. Part II: Seismic response, Earthquake Engng. Struct. Dyn. **29**, 499 (2000).
18 R. F. Fung, L. Y. Lu, and S. C. Huang, Dynamic modelling and vibration analysis of a flexible cable-stayed beam structure, J. Sound Vib. **254**, 717 (2002).
19 M. H. Wei, Y. Q. Xiao, and H. T. Liu, Bifurcation and chaos of a cable-beam coupled system under simultaneous internal and external resonances, Nonlinear Dyn **67**, 1969 (2012).
20 L. Wang, X. Zhang, S. Huang, and L. Li, Measured frequency for the estimation of cable force by vibration method, J. Eng. Mech. **141**, 06014020 (2014).
21 Z. Wang, C. Sun, Y. Zhao, and Z. Yi, Modeling and nonlinear modal characteristics of the cable-stayed beam, Eur. J. Mech.-A Solids **47**, 58 (2014).
22 Z. Yi, L. Wang, and Y. Zhao, Nonlinear dynamic behaviors of viscoelastic shallow arches, Appl. Math. Mech.-Engl. Ed. **30**, 771 (2009).
23 N. Malhotra, and N. S. Namachchivaya, Chaotic motion of shallow arch structures under 1:1 internal resonance, J. Eng. Mech. **123**, 620 (1997).
24 N. Malhotra, and N. S. Namachchivaya, Chaotic dynamics of shallow arch structures under 1:2 resonance, J. Eng. Mech. **123**, 612 (1997).
25 H. J. Kang, T. D. Guo, Y. Y. Zhao, W. B. Fu, and L. H. Wang, Dynamic modeling and in-plane 1:1:1 internal resonance analysis of cable-stayed bridge, Eur. J. Mech.-A Solids **62**, 94 (2017).
26 Y. Cong, H. Kang, and T. Guo, Planar multimodal 1:2:2 internal resonance analysis of cable-stayed bridge, Mech. Syst. Signal Processing **120**, 505 (2019).
27 Z. Yi, L. Wang, H. Kang, and G. Tu, Modal interaction activations and nonlinear dynamic response of shallow arch with both ends vertically elastically constrained for two-to-one internal resonance, J. Sound Vib. **333**, 5511 (2014).
28 A. W. Leissa, and M. S. Qatu, Vibrations of Continuous Systems (McGraw-Hill, New York, 2011).
29 Z. Liu, J. Niu, and R. Jia, Dynamic analysis of arbitrarily restrained stiffened plate under moving loads, Int. J. Mech. Sci. **200**, 106414 (2021).
30 Z. Yi, and I. Stanciulescu, Nonlinear normal modes of a shallow arch with elastic constraints for two-to-one internal resonances, Nonlinear Dyn. **83**, 1577 (2016).
31 Y. L. Pi, M. A. Bradford, and F. Tin-Loi, Nonlinear analysis and buckling of elastically supported circular shallow arches, Int. J. Solids Struct. **44**, 2401 (2007).
32 M. H. Wei, Y. Q. Xiao, H. T. Liu, and K. Lin, Nonlinear responses of a cable-beam coupled system under parametric and external excitations, Arch. Appl. Mech. **84**, 173 (2014).
33 D. Q. Cao, M. T. Song, W. D. Zhu, R. W. Tucker, and C. H. T. Wang, Modeling and analysis of the in-plane vibration of a complex cable-stayed bridge, J. Sound Vib. **331**, 5685 (2012).
34 E. Mettler, Dynamic buckling, in Handbook of Engineering Mechanics, edited by W. Flügge (McGraw-Hill, New York, 1962).
35 Z. P. Yi, H. J. Kang, and L. H. Wang, Research on the nonlinear dynamic behaviors of elastic support shallow arch, J. Dyn. Control. **11**, 48 (2013).
36 E. Özkaya, M. Sarigül, and H. Boyaci, Nonlinear transverse vibrations of a slightly curved beam carrying a concentrated mass, Acta Mech. Sin. **25**, 871 (2009).
37 R. Seydel, Practical Bifurcation and Stability Analysis (Springer, New York, 2009).
38 A. H. Nayfeh, and B. Balachandran, Applied Nonlinear Dynamics (Wiley, New York, 1995).
39 W. Hu, J. Ye, and Z. Deng, Internal resonance of a flexible beam in a spatial tethered system, J. Sound Vib. **475**, 115286 (2020).
40 L. Q. Chen, Y. L. Zhang, G. C. Zhang, and H. Ding, Evolution of the double-jumping in pipes conveying fluid flowing at the supercritical speed, Int. J. Non-Linear Mech. **58**, 11 (2014).

两端具有弹性支承双索浅拱模型的内共振分析

苏潇阳, 康厚军, 郭铁丁, 闫桂荣

摘要 在以往关于斜拉桥非线性动力学的研究中, 边界条件并没有被合适地模拟. 为了更准确地探索斜拉桥的非线性动力学特性, 论文考虑斜拉桥的初始构型, 建立了两端具有弹性支承的双索浅拱模型. 首先, 将浅拱根据拉索的数量分为三段, 对模型的面内特征值问题进行求解, 并将求得的分段函数作为浅拱的试函数. 其次, 对浅拱发生主共振时全局模态和局部模态间的1:1:1内共振进行研究. 采用伽辽金方法得到系统的常微分方程, 并通过多尺度法进行求解. 采用牛顿-拉夫逊方法得到调谐方程的稳定平衡解, 并给出不同竖向刚度下模型的频率/力响应曲线, 从而对模型的非线性行为进行分析. 最后, 基于以上研究得出一些有意义的结论.